

Normalized Difference Flood Index for rapid flood mapping: Taking advantage of EO big data



Fabio Cian^{a,b,*}, Mattia Marconcini^c, Pietro Ceccato^d

^a Department of Economics, University Ca' Foscari of Venice, Venice, Italy

^b Venice Centre for Climate Studies (VICCS), Venice, Italy

^c DFD German Aerospace Center (DFD-DLR), Wessling, Germany

^d International Research Institute for Climate and Society (IRI), Columbia University, New York, USA

ARTICLE INFO

Keywords:

SAR
Flood mapping
EO big data
Flood index
Multi-temporal statistics

ABSTRACT

Climate change projections foresee an increasing number of intense precipitation events with consequent flash and riverine floods. An accurate and rapid mapping of these phenomena is a key component of effective emergency management and disaster risk reduction plans. Earth Observation big data such as the ones acquired by the Copernicus programme, are providing unprecedented opportunities to detect changes and assess economic impacts in case of disasters.

This paper presents an innovative flood mapping technique based on an index which is computed using multi-temporal statistics of Synthetic Aperture Radar images. The index compares a large amount of reference scenes to those acquired during the investigated flood and allows an easy categorization of “flooded” areas; either areas solely temporarily covered by water or areas with mixed water and vegetation. The method has been developed specifically to exploit Sentinel-1 data but can be applied to any other sensor. It has been tested for the 2010 flood of Veneto (Italy) and the floods of 2015 in Malawi and Uganda. Extensive qualitative analysis and cross-comparison with other state-of-the art methods, proved the proposed approach highly reliable and particularly effective, allowing a precise, simple and fast flood mapping. Compared to the maps produced for emergency management for the event analyzed, we obtained an overall agreement of 96.7% for Malawi and an average of 96.5% for Veneto for the 5 maps presented.

1. Introduction

New satellite constellations, such as the European Space Agency's (ESA) Sentinels, have started the era of Earth Observation (EO) big data (Hua-Dong et al., 2015; Ma et al., 2015; Yang et al., 2017) allowing to entering a new paradigm for disaster monitoring and EO data exploitation. Sentinel-1 (S1), a constellation of two radar satellites operational since October 2014, can monitor the entire Earth every 6 days, giving an unprecedented opportunity to access a large number of archived scenes (Potin et al., 2015; Torres et al., 2012). This allows statistical analysis to be performed on long time-series of data and new approaches in change detection (CD) analyses to be developed for mapping floods, assessing their economic impacts and managing emergency responses.

With a foreseen increase in the number of extreme precipitation events due to climate change and consequent flash and riverine floods (MunichRE, 2014), rapid and accurate mapping of floods is of key importance. Firstly, rapidity is key in emergency management (EM),

with new cloud computing tools (Yue et al., 2013; Li et al., 2015; Yang et al., 2013) such as Google Earth Engine (GEE) (Google Earth Engine, Google, n.d.) starting to play a fundamental role (Karamouz et al., 2013). Secondly, accuracy is required not only in EM, but also for better planning urban areas, for saving lives, for reducing economic losses and building more resilient livelihoods (de Moel et al., 2015; Mysiak and Luther, 2013; UNISDR, 2015). The big EO data of ESA's Copernicus programme is helping to move towards an improved flood risk assessment for both EM and better infrastructure planning (Twele et al., 2016).

The capability of near-real time flood mapping by means of EO data has already been demonstrated in the past (Horritt et al., 2001; Matgen et al., 2007; Brisco et al., 2011; Henry et al., 2006; Cossu et al., 2009; Martinis et al., 2015) and it is now regularly used by operational emergency response centers (Bassis et al., 2004; Mahmood, 2012) such as the European Copernicus Emergency Management Service (Copernicus EMS) or the International Charter on Space and Major Disaster (International Charter, n.d.).

* Corresponding author at: Department of Economics, University Ca' Foscari of Venice, Venice, Italy.

E-mail addresses: fabio.cian@unive.it (F. Cian), mattia.marconcini@dlr.de (M. Marconcini), pceccato@iri.columbia.edu (P. Ceccato).

Table 1

Summary of relevant literature in flood mapping in chronological order from the year 2000. The table specifies the data used, location, type of environment, size of the study area, method and key results. The last column (Key Results) reports “Quantitative result not available” whenever the study did not provide any quantitative results in terms of flood map extent accuracy. For the sake of completeness, the proposed method has been added in the last row.

Study	Data used/res./band	Location/landscape/study size/dates	Method/approach	Key results
1 - (Nico et al., 2000)	ERS-1/2/30 m/C	Béziers, France/urban, agricultural areas/10.000 km ² /January 1996	Interferometric coherence change detection	<ul style="list-style-type: none"> - Combined use of amplitude and interferometric coherence improved detection of flood compared to the use of amplitude only - Quantitative result not available
2 - (Horritt et al., 2001)	ERS-1/30 m/C	Oxford, UK/agricultural areas/250 km ² /December 1992	Active contour model	<ul style="list-style-type: none"> - Discrimination of thickly vegetated areas from flooded areas - 75% accuracy with respect to simultaneous aerial photo
3 - (Brivio et al., 2002)	ERS-1/30 m/C	Piedmont region, Italy/flat agricultural area/450 km ² /November 1994	Thresholding + DEM filling	<ul style="list-style-type: none"> - Estimation of flood peak extent - 96.7% map accuracy with respect to the official map created by the local government
4 - (Bazi et al., 2005)	ERS-2/30 m/C	City of Bern, Switzerland/urban, alpine/80 km ² /May 1999	Unsupervised change detection	<ul style="list-style-type: none"> - Automatic unsupervised filtering and threshold selection - Simple and stable method - Accuracy similar to manual supervised thresholding - Quantitative result not available
5 - (Henry et al., 2006)	1) ENVISAT-ASAR/30 m/C 2) ERS-2/30 m/C	Elbe River, Dresden, Germany/urban, agricult. areas/~/August 2002	Thresholding	<ul style="list-style-type: none"> - Comparison of different polarization for flood detection - HH more suitable for flood detection compared to VV - HV improve the detection if combined with HH - 85% agreement with map derived from Landsat 7 - Automatic extraction of flooded area taking into consideration terrain elevation - The use of elevation data combined with SAR improved the accuracy - Quantitative result not available
6 - (Mason et al., 2007)	ERS-1/30 m/C and LiDAR DTM/2 m	Oxford, UK/flat agricultural area/40 km ² /December 1992	Active contour model on SAR and DTM	<ul style="list-style-type: none"> - The use of elevation data combined with SAR improved the accuracy - Quantitative result not available - The use of elevation data combined with SAR improved the accuracy - Extraction of flood in vegetated areas - Quantitative result not available
7 - (Matgen et al., 2007)	1) ENVISAT-ASAR/30 m/C 2) LiDAR DEM/2 m	River Alzette, Luxembourg/urban, alpine/30 km ² /January 2003	Thresholding + active contour model	<ul style="list-style-type: none"> - Unsupervised flood detection using locally computed thresholds - Computationally efficient compared to global thresholding - Operational rapid mapping - Use of DEM for improving accuracy - 95.5% overall accuracy on a subset of the dataset with respect to ground truth of the event - Quantitative result not available
8 - (Martinis et al., 2009)	TerraSAR-X/3 m/X	Tewkesbury, UK/urban, agricult. areas/1.500 km ² /July 2007	Thresholding + segmentation	<ul style="list-style-type: none"> - The use of elevation data combined with SAR improved the accuracy - Quantitative result not available - The use of elevation data combined with SAR improved the accuracy - Extraction of flood in vegetated areas - Quantitative result not available
9 - (Schumann et al., 2010)	ENVISAT-ASAR/150 m/C	Po river, Cremona, Italy/urban, agricultural areas/1.250 km ² /June 2008	Thresholding + hydrologic modelling	<ul style="list-style-type: none"> - Verification of flood inundation models in near-real time - Quantitative result not available
10 - (Maignen et al., 2011)	ENVISAT-ASAR/150 m/C Radarsat-1/25 m/C	1) Red river, US/urban, agric. areas/4.500 km ² /April 1997 2) Tewkesbury, UK/urban, agric. areas/800 km ² /July 2007	Thresholding + region growing and change detection	<ul style="list-style-type: none"> - Automatic, objective and reliable flood mapping - 85% overall accuracy with respect to a map extracted from aerial photography - Delination of flood water using high incidence angle SAR images - Retrieval of optimal threshold values - Quantitative result not available
11 - Manjusree et al. (2012)	Radarsat-2/50 m and 3 m/C	Kosi subbasin, Darbhanga District, Bihar State, India/monsoonal climate, agricultural areas/25.000 km ² /October 2011	Thresholding based on incidence angle	<ul style="list-style-type: none"> - Automatic near-real time flood mapping in rural-urban areas - 89% overall accuracy with respect to aerial photographic data - Automated, objective and repeatable flood detection in urban areas - 82% overall accuracy with respect to aerial photography-derived flooded areas - Discrimination of artifacts caused by heavy rain or wet snow cover - Quantitative result not available
12 - (Mason et al., 2012a, 2012b)	TerraSAR-X/3 m/X	Tewkesbury, UK/urban and rural flooding/70 km ² /July 2007	Thresholding + segmentation	<ul style="list-style-type: none"> - Automated, objective and repeatable flood detection in urban areas - Frequency of flooding - Quantitative result not available
13 - (Giustarini et al., 2013)	TerraSAR-X/3 m/X	Severn River, Tewkesbury, UK/urban areas/3 km ² /July 2007	Thresholding, region growing, change detection	<ul style="list-style-type: none"> - Automated, objective and repeatable flood detection in urban areas - Frequency of flooding - Quantitative result not available
14 - Pulfienti et al. (2014)	COSMO-SkyMed/3 m/X	Northwest Italy/urban, alpine, agricultural areas/1.700 km ² /November 2011	Segmentation + fuzzy logic	<ul style="list-style-type: none"> - Data fusion of optical and radar data - Understanding of floodplain inundation dynamics - Flood in vegetated areas
15 - Long et al. (2014)	ENVISAT-ASAR/150 m/C and Radarsat-2/6.25 and 12.5 m/C	Caprivi region, Namibia/tropical rural areas, wetlands/10.000 km ² /March 2009, March 2011, April 2012, March 2013	Change detection + thresholding	<ul style="list-style-type: none"> - Simple and fast method - Flood in vegetated areas - Frequency of flooding - Quantitative result not available
16 - (Ward et al., 2014)	ALOS-PALSAR/100 m/L Landsat TM 5/30 m/optical	Alligator Rivers region, northern Australia/wet-dry tropical floodplains/10.000 km ² /April to October 2009	Classification tree using spectral indices and segmentation	<ul style="list-style-type: none"> - Data fusion of optical and radar data - Understanding of floodplain inundation dynamics - Flood in vegetated areas

(continued on next page)

Table 1 (continued)

Study	Data used/res./band	Location/landscape/study size/dates	Method/approach	Key results
17 - (Martinis et al., 2015)	TerraSAR-X/3 m and 8.25 m/ X	1) Schkopau, Germany/1 km ² /July 2011 2) Shkodër, Albania and Scutari, Montenegro/ 14.500 km ² /March 2013 3) Bangkok, Thailand/1 km ² /November 2011	Thresholding + fuzzy logic + region growing	- 86% classification accuracy and 93% overall accuracy with respect to ground control points - On-demand automatic flood mapping service - Effective for different types of SAR data - Overall accuracy for three case studies of 91.6%, 87.5% and 99.4% with respect to a flood map obtained by visual interpretation of digital aerial images
18 - (Pulvirenti et al., 2016)	COSMO-SkyMed/3 m/X	Emilia-Romagna region, Italy/urban, agricultural areas/300 km ² /January 2014	Interfere, coherence change detection + region growing	- Analysis of multitemporal trends of coherence, improved mapping of flood in vegetated and urban areas - Quantitative result not available - Probability of flooding - Uncertainty of flood extent - Quantitative result not available
19 - (Giustarini et al., 2016)	1) ENVISAT-ASAR/150 m/C 2) TerraSAR-X/3 m/X 3) Radarsat-1/25 m/C	1) Red river, US/urban, agricultural areas/ 4.500 km ² /April 1997 2) Tewkesbury, UK/urban, agricultural areas/ 800 km ² /July 2007	Probabilistic flood mapping (Bayesian inference)	- Reliable flood probability maps - Quantitative result not available - Robust, objective methodology suitable for different sensors - Detection of shallow water in short vegetation - Overall agreement of 96.7% for Malawi, 96.5% for Veneto on average for the 5 maps presented, with respect to maps produced by emergency management services for the events
20 - (Schlaifer et al., 2017)	ENVISAT-ASAR/150 m/C	Tewkesbury, UK/urban, agric. areas/20.000 km ² /July 2007	Probabilistic change detection	- Multi-temporal statistics + thresholding
21 - This study	1) Sentinel-1/20 m/C 2) CSK/3 m/X 3) TSX/3 m/X 4) RS-2/25 m/C 5) ENVISAT-ASAR/150 m/C	1) South Malawi/rural, agricultural areas/ →/January 2015 2) Veneto, Italy/urban, agricultural areas/ →/November 2010 3) Uganda/rural agricultural areas/November, December 2015		

Synthetic Aperture Radar (SAR) is particularly useful for flood mapping since it can provide frequent observations (Alsdorf et al., 2007; Mertes, 2002; Ward et al., 2014) thanks to the capability to monitor land in almost any weather conditions (Franceschetti and Lanari, 1999; Marzano et al., 2011; Schumann et al., 2009) and during night-time (O'Grady et al., 2011; Waisurasingha et al., 2007; Wilson and Rashid, 2005). SAR has been used since decades to extract information about floods by means of different reliable and well consolidated methodologies such as unsupervised classification, active contour models, CD and thresholding (Martinis et al., 2011; Horritt et al., 2001; Li et al., 2014; Hostache et al., 2012; Martinez and Le Toan, 2007; Pulvirenti et al., 2011; Pierdicca et al., 2013; Pulvirenti et al., 2013; Arnesen et al., 2013; Dellepiane et al., 2000; Dellepiane and Angiati, 2012; Bazi et al., 2005; Brivio et al., 2002; Di Baldassarre et al., 2011; Horritt, 1999; Mason et al., 2007; Matgen et al., 2007; Nico et al., 2000; Schumann et al., 2009; Smith, 1997). Table 1 summarizes key literature in flood mapping. Specifically, for each of the state of the art techniques, we list the corresponding data used for testing, along with specific characteristics of the landscape analyzed, the method employed and key results. It is worth noting that quantitative results are not available for every study.

Among these, image thresholding, which sets as flooded all the pixels with a radar backscatter lower than a certain threshold value (Mason et al., 2012a, 2012b; Pulvirenti et al., 2012; Schumann et al., 2010; Townsend, 2002), is computationally not demanding, provides reliable results and is ideal for rapid mapping. However, it is affected by sources of error typical of SAR flood mapping: 1) atmospheric disturbances (Atlas and Moore, 1987; Danklmaier and Chandra, 2009a, 2009b; Jameson et al., 1997; Polverari et al., 2014); 2) Bragg resonance in presence of wind (Bragg, 1913; Schaber et al., 1997); 3) double-bounce due to emerging vegetation or buildings from the inundated area (Franceschetti et al., 2002; Hong and Wdowinski, 2014; van Zyl et al., 1987; Hajnsek et al., 2009); 4) dry and smooth bare soil exhibiting backscatter similar to that of water surfaces (O'Grady et al., 2011); 5) vegetation masking part of the flood; 6) soil moisture content increasing radar backscattering and limiting flood detection in mixed pixel (Jackson et al., 1996; Paloscia et al., 2013; Quesney et al., 2000; Shoshany et al., 2000; Wagner et al., 1999); and 7) user-dependence of the parameters chosen to produce the map (Martinis et al., 2009). CD techniques are interesting because they can overcome part of these limitations and can substantially improve the accuracy of flood maps (Matgen et al., 2011). In CD techniques, the selection of a suitable reference image is crucial (Hostache et al., 2012) to detect changes in radar backscattering due to floods (Liu et al., 2004; Lu et al., 2004) and avoid the risk of under estimating the extent of the event (Singh, 1989; Lunetta et al., 2004; Ulaby and Dobson, 1989). By selecting reference images sensed with the same acquisition geometry of the flood image, it is possible to discriminate areas of low backscattering from flooded ones (Giustarini et al., 2013). However, for practical reasons the first non-flood image found in the archive is usually employed as reference (Jones et al., 2009). Now, thanks to EO big data we have the possibility of statistically analyzing long image time-series and easily identify a more robust reference.

An interesting attempt to merge the advantages of both CD and thresholding is presented by Long et al. (2014) who computed the absolute difference between the flood and reference images and then applied two thresholds for isolating both flood and shallow water in short vegetation. For limiting user dependence, the threshold values are determined analyzing the histogram of the difference image by means of a mathematical formula. However, here a coefficient needs to be determined by an analyst after several iterations, hence making the effectiveness of this approach still strongly user-dependent and highly variable depending on the specific case analyzed.

Following a similar approach, we developed a method for flood mapping characterized by a novel approach to CD; in particular, it is based on multi-temporal series analysis and the computation of two

new indices, i.e. the Normalized Difference Flood Index (NDFI) for highlighting flooded areas, and the Normalized Difference Flood in short Vegetation Index (NDFVI) for highlighting shallow water in short vegetation.

Main objectives of the designed approach – specifically designed for supporting disaster management and flood risk assessment – are:

- i) Robustness and simplicity (i.e., it requires the minimum amount of user-dependent input and is effectively applicable in different environments with data acquired by different sensors);
- ii) Exploitation of cloud computing and EO big data for improving CD through a more robust reference statistics;
- iii) Easy threshold selection through the use of normalized indices; and
- iv) Capability of outlining shallow water in short vegetation in addition to open-land flooded areas (information usually not reported by emergency mapping services, nevertheless crucial for emergency response plan, as well as for estimating impacts on agricultural activities).

2. Methodology

In this section we first present the implemented technique, which consists in the computation of the abovementioned NDFI and NDFVI, followed by thresholding and post-classification. Then, a comprehensive analysis is given for the two indices.

2.1. NDFI and NDFVI extraction

S1 is observing the Earth systematically with a revisiting frequency of 6 days, leading to a large amount of reference pre/post event scenes in addition to those acquired during the investigated flood. S1 acquires with a stable incidence angle, therefore all the images on the same orbit track can be directly compared as they exhibit same shadowing and layover effects. Our method exploits this large amount of information by: i) performing a statistical analysis of the time-series to better characterize the behaviour of each pixel; and ii) using normalized indices which help to effectively compress information on long time-series.

As summarized in Fig. 1, two SAR multi-temporal series are created: one containing only reference images and one containing also images of the flood under investigation. The two stacks are first radiometrically calibrated and terrain corrected. Statistical analysis of the backscattering σ_0 of each pixel is then performed throughout the whole multi-temporal series. For each pixel, we calculate the minimum, maximum and mean, for both the stack of reference images and the one

also including the flood scenes. The calculated temporal statistics are used to compute the NDFI, which aims at highlighting temporary open water bodies:

$$\text{NDFI} = \frac{\text{mean } \sigma_0(\text{"reference"}) - \min \sigma_0(\text{"reference + flood"})}{\text{mean } \sigma_0(\text{"reference"}) + \min \sigma_0(\text{"reference + flood"})}. \quad (1)$$

NDFI easily allows us to categorize as “flooded” those areas solely temporarily covered by water with respect to permanent water bodies and non-water land cover classes. The mean value of each pixel in the reference stack represents the average behaviour of the land surface. For instance, permanent water surfaces exhibit a low mean value even though some pixels could assume medium-high backscatter in one image, for example due to the presence of wind. Smooth surfaces such as roads or airport runways have backscatter mean values close to zero. All non-smooth surfaces (e.g. urban areas, forests and agriculture) have a mean value well above zero. The minimum value of each pixel in the stack containing the flood images is used to capture a specific discontinuity in the time series, i.e. those pixels that during the flood exhibit very low backscatter. The difference between the mean and the minimum value highlights those discontinuities, i.e. flooded areas. Normalizing the difference allows us to have values between 0 and 1 and helps to define a threshold to mask flooded areas.

All unchanged features in the index image have their value close to zero and can easily be masked, including permanent water bodies and non-water pixels with low backscattering such as roads, dry bare soil, and smooth tarmac that do not change their backscatter significantly. To detect shallow water in short vegetation, a different index is created aiming at highlighting the increase of backscatter that happens in those circumstances. Using the statistics on the stacks, the Normalized Difference Flood in Vegetated areas Index (NDFVI) is computed:

$$\text{NDFVI} = \frac{\max \sigma_0(\text{"reference + flood"}) - \text{mean } \sigma_0(\text{"reference"})}{\max \sigma_0(\text{"reference + flood"}) + \text{mean } \sigma_0(\text{"reference"})}. \quad (2)$$

In this case the maximum value of the pixels aims at highlighting the discontinuity in the time-series caused by shallow water in short vegetation. The difference with the mean value highlights only those pixels that experience a strong increase in their backscatter.

2.2. Thresholding

After the computation of the two indices, a suitable threshold value has to be identified to solely extract flooded areas. Long et al. (2014) find the threshold analyzing the histogram of the difference image, i.e. reference image minus the image of the flood. The threshold is the mean value of the whole difference image minus k times the standard

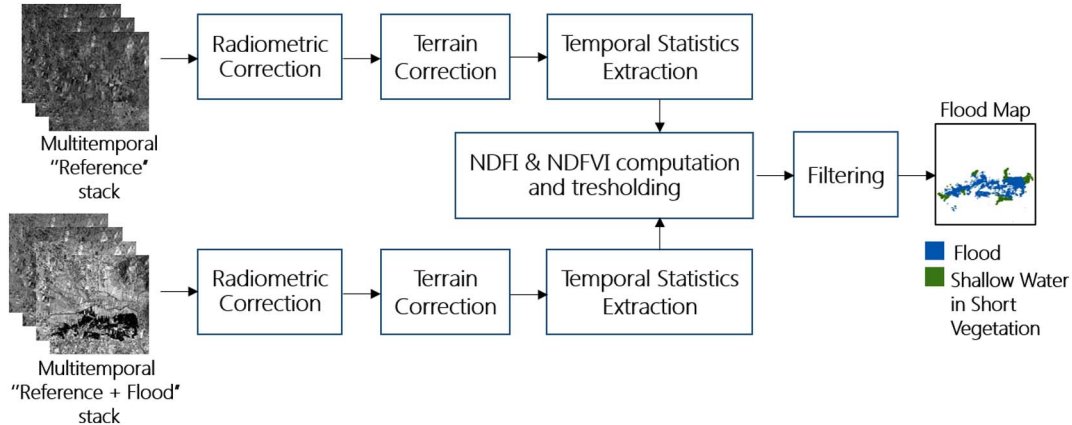


Fig. 1. The methodology proposed consists in creating two stacks of images: one containing only reference images and one containing also images of the flood under investigation. The two stacks are then radiometrically calibrated and terrain corrected. Temporal statistics are extracted to compute the Normalized Difference Flood Index (to highlight temporary open water bodies) and the Normalized Difference Flood in Vegetated areas Index (to highlight shallow water in short vegetation). A threshold is finally applied to the indices values to extract only flooded areas. Additional filtering is applied to remove spurious cluster of pixels.

deviation. Following a similar approach, we analyzed the NDFI values over areas more likely to be flooded and computed the same metric:

$$th = \text{mean}(\text{NDFI}_{\text{flood}}) - k * \text{std}(\text{NDFI}_{\text{flood}}). \quad (3)$$

After empirical analysis of several test cases, a value that proved to be particularly effective is $k = 1.5$, which led to a threshold of 0.7 for the NDFI. Hence, this is the value we suggest as optimal, which might be fine-tuned by the user for particular cases. This value is conservative to obtain a clean map. In fact, pixels with NDFI values in the proximity of the threshold can also be found in dry bare soil, shadow or other smooth surfaces mainly due to the effect of the speckle. Decreasing the threshold would result in more false alarms. On the other hand, transitional pixels (pixels at the boarders of flooded area or partly inundated ones) can be excluded by the threshold since they could have a smaller value of NDFI.

The same approach has been followed for the NDFVI, where the suggested threshold is 0.75, obtained using $k = 1.5$:

$$th_v = \text{mean}(\text{NDFVI}_{\text{flood, veg}}) + k_v * \text{std}(\text{NDFVI}_{\text{flood, veg}}). \quad (4)$$

2.3. Post-processing

The maps obtained after the thresholding are then filtered following the scheme in Fig. 1 to reduce three sources of errors. Firstly, to reduce the effect of speckle, the classified image is segmented and filtered using two morphological filters: i) dilate filter which gradually enlarges the boundaries of regions of foreground pixels, followed by ii) closing filter which removes small holes while preserving boundaries (Gonzalez and Woods, 2007). Both filters use a window of 3 by 3 pixels, which is identified as suitable solution based on empirical analysis. Secondly, all clusters smaller than 10 pixels are excluded to reduce spurious flooded areas. Thirdly, the pixels falling in a slope of $> 5^\circ$, where a flood would be unlikely, are excluded. Slopes are computed using Digital Elevation Models.

The two morphological filters allowed us to include in the map flooded pixels that have slightly lower NDFI values but still with high probability to be part of the flood, i.e. pixels at the boarders of the flooded areas or pixels surrounded by flood, without adding noise to the map. A longer time-series of images reduce this uncertainties since the speckle effect is averaged in the temporal statistics.

The same post-processing steps are applied to all the different datasets used in this analysis.

2.4. NDFI analysis

To better understand the NDFI, we analyzed all the possible values that the index might take based on extensive experimental analysis. We partitioned NDFI into different subsets. In Fig. 2(a) we plotted the minimum value of σ_0 ("reference + flood") in the x-axis and the mean value of σ_0 ("reference") in the y-axis. The index exhibits constant values along isolines starting from the origin. The value corresponding to each isoline is indicated in the upper x-axis. The plane is then divided in two regions by the diagonal (isoline equal to 0); the area below it and marked as (1), corresponds to negative values of NDFI that are unlikely since we expect the mean value of the reference stack to be always greater than the minimum value of the stack containing the flood images and we can exclude it from our analysis.

The area above the diagonal is divided in two by the suggested threshold isoline (NDFI = 0.7): area (2) correspond to the pixels selected as flooded and area (3) to non-flooded ones. On the NDFI isoline equal to 0 lay permanent water bodies and stable features such as urban areas, roads, smooth tarmac and desert. In particular, permanent water bodies should lie close to the origin of the plot since they have very low backscatter values. In practice, since small fluctuations of backscatter values can occur caused by speckle and little variations at the surface,

permanent water bodies lay on area (A) represented by the small blue and white triangle.

Fig. 2(b) zooms on area (A) of the plot considering values of $\sigma_{0\text{mean}}$ from 0 to 0.03. It shows how the threshold applied on the NDFI includes part of this area in the flood map (left side of the blue threshold line, i.e. for NDFI values > 0.7). The area included in the map can be divided in two further areas: (2A) where the mean value of the reference $\sigma_{0\text{mean}}$ is smaller than 0.015 (value representing only water pixel) and area (2B) with $\sigma_{0\text{mean}} > 0.015$ (water with greater backscattering and dry bare soil). Area (2A) is generally associated to permanent water bodies wrongly included in the flood map. Area (2B) mainly represents dry bare soils that decrease their backscatter during the flood and therefore it is correct to include them in the flood map.

In Fig. 2(c), the red dashed line ($\sigma_{0\text{min}} = 0.03$) represents the maximum backscatter for water pixels in the stack containing the flood images. Excluding area (A), it creates 3 additional areas in the NDFI plot. Area (2C) represents non-water pixels (medium-high backscattering, $\sigma_{0\text{mean}} > 0.03$) that strongly decrease their backscatter during the flood ($\sigma_{0\text{min}} < 0.03$), i.e. they are the flooded pixel included in the flood map. Area (2D) represents pixels that could be wrongly included in the final flood map since they consistently decrease their backscatter during the flood, indicating that something happened, but not enough to reach a $\sigma_{0\text{min}}$ typical of water pixels. In fact in this area we could include pixels with $\sigma_{0\text{min}}$ equal up to 0.176. This error is negligible since normally few pixels show this behaviour. Area (3A) represents non-water pixels with low reference backscattering ($0.03 < \sigma_{0\text{mean}} < 0.17$) that slightly decrease their backscatter during the flood ($0.015 < \sigma_{0\text{min}} < 0.03$). In Fig. 2(d), we can see in details this part of the plot. The line $\sigma_{0\text{min}} = 0.015$ divides area (3A) in two sub-regions. Area (3A.1) can contain flooded areas with a fairly low mean backscattering in the reference. Decreasing the value of the NDFI threshold would include these flooded pixels in the flood map but also increase false-alarms. We used morphological filters to include those flooded pixels without increasing noise. Most of the pixels belonging to this area are correctly excluded from the map. Area (3A.2) is composed of pixels at the boundaries of water surfaces or bare soils that decrease their backscattering during the flood. The remaining part of area (3) is correctly excluded by the index threshold since those are pixels that decrease their backscatter but that are surely not water pixels since their $\sigma_{0\text{min}}$ is too high ($\sigma_{0\text{min}} > 0.03$).

2.5. NDFVI analysis

Fig. 3(a) shows the values of NDFVI for a given couple ($\sigma_{0\text{mean}}$ ("reference"), $\sigma_{0\text{max}}$ ("reference + flood")). As in the NDFI case, the isoline equal to 0 divides the plane in two areas, where area (V1) corresponds to unlikely negative index values and therefore is excluded from our analysis. Area (V2) represents the pixels included in the flood map ($\text{NDFVI} > 0.75$) and area (V3) the ones excluded. Fig. 3(b) analyses in detail area (VA), which is a subset of area (V2) where $\sigma_{0\text{mean}}$ exhibits low values (< 0.5). Area (V2A) represents pixels with very low values ($\sigma_{0\text{mean}} < 0.015$, most likely water) that increase more or less consistently their backscatter during the flood. Part of this increment is due to fluctuation of the backscattering over permanent water bodies meaning that we would include a very small part of these in the final map. Instead, when the increment is very high, most probably it is due to the effect of wind or vegetation in water surfaces. Area (V2B) represents non-stable water surfaces or very dry bare soil that increase the backscatter during the flood. Area (V2C) and the remaining of area (2) represent herbaceous or shrub areas that experience the same phenomenon, most probably the effect of shallow water or increased soil moisture. These two areas are correctly included in the map.

3. Results

The method was tested using three different case studies: i) the flood

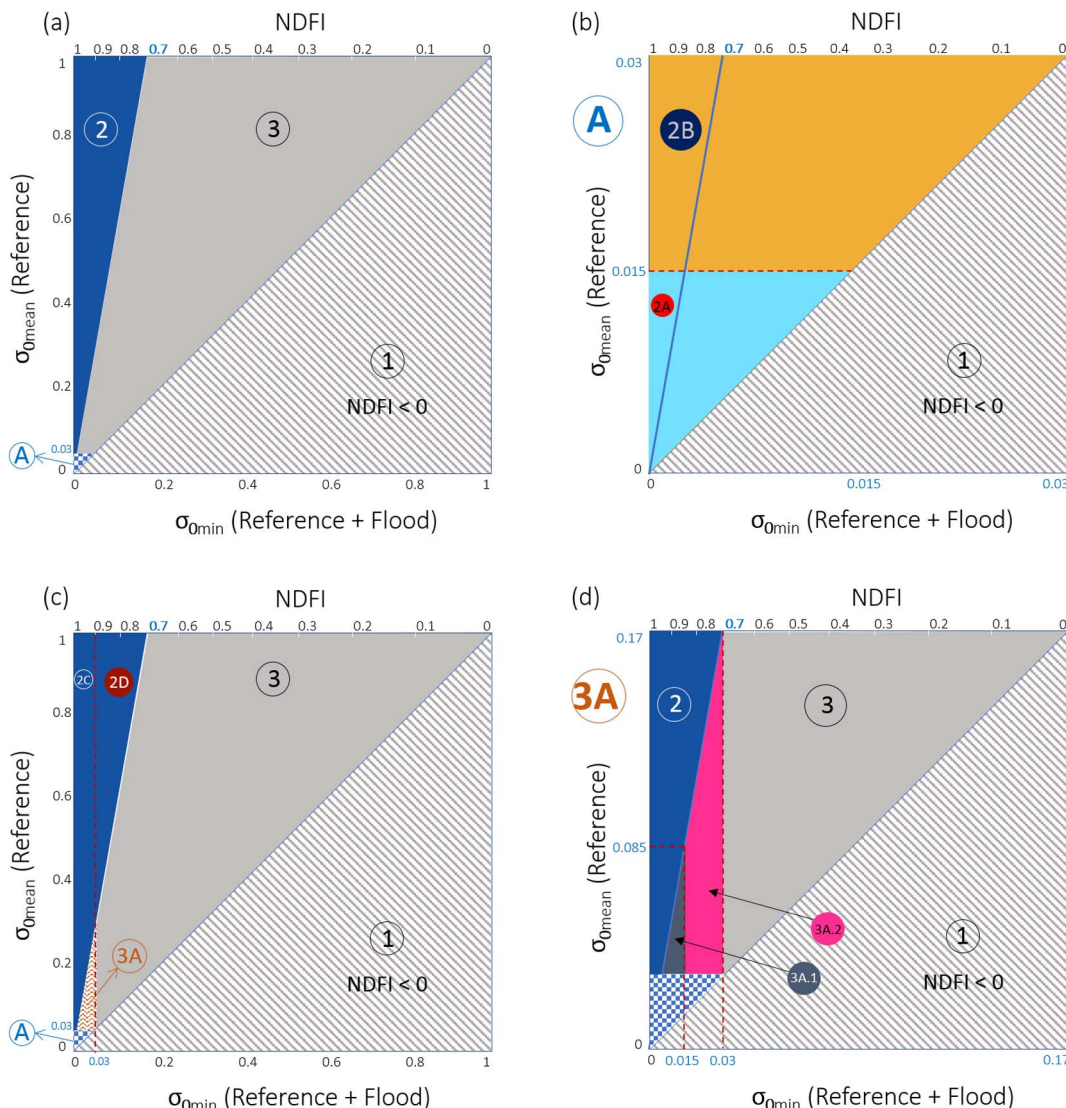


Fig. 2. Normalized Difference Flood Index (NDFI) analysis: index values are plotted with reference to the minimum pixels intensity (in linear scale) throughout the “reference + flood” multi-temporal series (x axis) and the mean pixel values (in linear scale) throughout the “reference” time series (y axis). (a) Area (1) is neglected since it indicates negative values of the NDFI. The blue area (2) indicates the values included in the flood map using the suggested thresholding of 0.7. Area (3) represents the values of NDFI not included by the thresholding. (b) Zoom on the area (A) of NDFI plot (small blue-white area in panel (a)). The threshold on the NDFI (0.7) includes part of the permanent water pixels (area (2A)). Area 2B represents instead dry bare soil that decreased its intensity due to flood. A careful analysis shows that this error represents only a small percentage of the total flood map. (c) The dashed line at $\sigma_{0\min} = 0.03$ divides area (2) in area (2C), flooded pixels and area (2D), non-flooded pixel. This error is negligible since very few pixels fall in this area. (d) Zoom on the area (3A) of NDFI plot. The threshold on the NDFI (0.7) excludes possible flooded areas: Area (3A.1), possible flood with low reference backscatter and area (3A.2), pixels at the boundaries of water surfaces. A careful analysis shows that this error is compensated by the morphological filtering steps and therefore acceptable. (For interpretation of the references to color in this figure legend, the reader is referred to the web version of this article.)

of January 2015 that occurred in southern Malawi captured by S1; ii) the flood event occurred in November 2010 in the Veneto region (city of Vicenza and its surroundings) in North Eastern Italy for which multi-temporal CSK stripmap data were used; this case study was chosen because it represents the typical situation of data availability before the advent of S1 images; iii) the flood occurred in North Eastern Uganda in November 2015 also well covered by S1 data.

3.1. Southern Malawi, 2015

At the beginning of January 2015, Malawi experienced exceptional rainfall, which led to a disastrous flood especially in the southern part of the country that lasted until the end of March. The amount of rainfall was the highest on records and the event constitutes a 500 year flood (Malawi, 2015). The already precarious situation for households, was exacerbated by the disaster. More than 1 million people were

affected, > 200 thousands displaced, > 100 killed (Malawi, 2015). In this study, we focus on analyzing the flooded areas for which S1 data were available, i.e. the southern district of Chikwawa and Nsanje as shown in Fig. 4(a) and (b).

3.1.1. Data used

Even if S1 was at the very beginning of its life and not at its full acquisition potential, the frequent observation strategy of the mission allowed us to access several images prior to the flood occurrence. Here, in selecting the images suitable to be taken as reference, it is important to take into consideration the climate of the region, which is sub-tropical, relatively dry and strongly seasonal.

To derive robust statistics, we took into consideration only the scenes acquired during the rainy season, which started in November 2014. Concerning the temporal coverage of the flood, except for the initial phase of the event (unfortunately the most important to

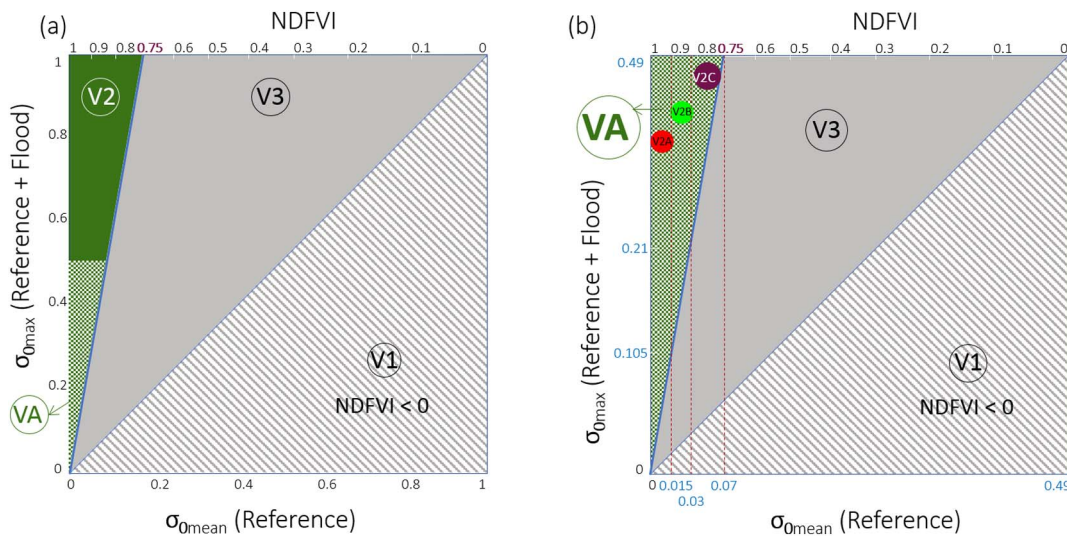


Fig. 3. Normalized Difference in Vegetation Flood Index (NDFVI) analysis: index values are plotted with reference to the minimum pixels intensity (in linear scale) throughout the “reference” multi-temporal series (x axis) and the mean pixel values throughout the “reference + flood” time series (y axis). (a) Area (1) is neglected since it indicates negative values of the NDFVI. The green area (V2 and VA together) indicates the values included in the flood map using a thresholding of 0.75. Area (V3) represents the values of NDFVI not included by the thresholding (b) Zoom on the area VA of NDFVI plot. This region can be divided into other 3 sub-regions depending on the mean backscatter in the reference images allowing to understand what it is mapped as shallow water by means of the threshold on the NDFVI. (For interpretation of the references to color in this figure legend, the reader is referred to the web version of this article.)

understand the maximum flood extent) when S1 did not yet systematically acquired over the study site, data were available every 12 days allowing to precisely monitor its evolution as shown in Table 2.

The Shuttle Radar Topography Mission (SRTM) DEM was used to filter steep areas.

3.1.2. Results

The frequent acquisition of S1 during the flood allowed us to derive 7 flood extent maps using the data listed in Table 2. Results for the surrounding of Bangula in the Chickwawa district, area (A), are reported in Fig. 4(c) for January 22, Fig. 4(d) for February 21, Fig. 4(e) for March 23. Results for the Nsanje district, area (B), are reported in Fig. 4(f) for January 22, Fig. 4(g) for February 21, Fig. 4(h) for March 23. The maps show flooded areas in blue and shallow water in short vegetation in green. They give an overview of the evolution of the flood in the three months of observations, from January 4, 2015, right before the start of the event, through January 22 that is the peak of the flood captured by S1, until March 23, at the end of the emergency.

The Copernicus EMS issued a map produced using the same data we used for the January 22 map. The map was produced by e-GEOS by means of their *e-FLOOD software, which relies on an unsupervised algorithms refined with smoothing and homogenization techniques built as a plug-in to the *ENVI platform (Ciappa et al., 2015; Grandoni et al., 2014). The nominal accuracy of the maps produced by e-GEOS in the frame of Copernicus EMS is 85% (Grandoni, 2013). However, accuracy values specific to the maps considered in this work were not available; moreover, these did not include any information about shallow water in short vegetation hence preventing the possibility of cross-comparison with our results.

The two products were compared over the area where they overlap as in Fig. 5(a–c), where we can see a high agreement between them. The main differences are due to permanent water bodies, as it can be seen in central bottom part of Fig. 5(c). Copernicus EMS product discarded permanent water bodies using ancillary data. Instead, we based our analysis only on the observations during the rainy season. Therefore, we reported as flooded all the areas that did not show as covered by water in the reference images. Vice versa, Copernicus EMS reported as flooded areas that we found already covered by water before the beginning of the flood. Table 3 shows the quantitative comparison, which reflects what can be observed in the maps: 71.6 km² were

reported as flooded in both maps, 37.1 km² only in the proposed method and 22.9 km² exclusively in the Copernicus EMS. Taking Copernicus EMS maps as a reference, the specific agreement on flooded areas is of 75.8% and the overall agreement of 96.7%.

For a further comparison, we decided to derive a map using Landsat-8 (L8) data. We used all the acquisitions over the area of interest (Landsat Paths 166 and 167, Rows 71, 72 and 73) with a cloud cover lower than 60%. The images were cloud masked and the Normalized Difference Flood Index (NDFI) was computed for each scene. For each pixel, we computed the minimum, maximum and mean of the NDVI throughout the whole stack of images. Finally, a threshold on the three bands was applied to derive the flood map. The idea behind this method is that whenever there is a flooded surface, the value of NDVI strongly decreases. The minimum values aim at capturing this anomaly. In fact, over permanent water bodies the three statistics have comparable low values, instead on flooded areas the maximum and the mean values follow the characteristic of the specific corresponding land cover. Therefore, combining these together we are able to understand where the floods occurred. It does not allow us to identify in which days the floods occurred, but it allows us to identify all pixels which have been flooded at least once. Fig. 5(d–f) shows the comparison for small areas of overlap between the two maps. In particular, in Fig. 5(d) we can see the NDFI-based flood map for the period January–March 2015, in Fig. 5(e) the NDVI-based flood map for the whole 2015, in Fig. 5(f) a cross-comparison of the two methods. The main limitation in the NDVI-based method is the cloud coverage and the longer revisit time of L8 (16-day). The lower part of Table 3 shows an agreement of 449 km², while 546 km² were reported only by the NDFI-based method. 79.6 km² were reported only by the NDVI-based method. The main sources of difference in this case is the different acquisition dates and the cloud coverage which affect the optical images.

3.1.2.1. Indices analysis. Fig. 6 shows the results of indices analysis: (a) shows a Google Earth image of the surrounding of the city of Nsanje; (b) the correspondent NDFI image; (c) the resulting flood map. For values of $\sigma_0 < 0.015$ only water pixel are detected. This leads to a detection of water bodies that leaves out only the outer borders. Increasing this threshold, dry bare soil pixels starts to be included. When $\sigma_0 = 0.03$, water bodies are delineated very precisely (i.e. the borders of water bodies are also included) but also dry bare soils are included as we can

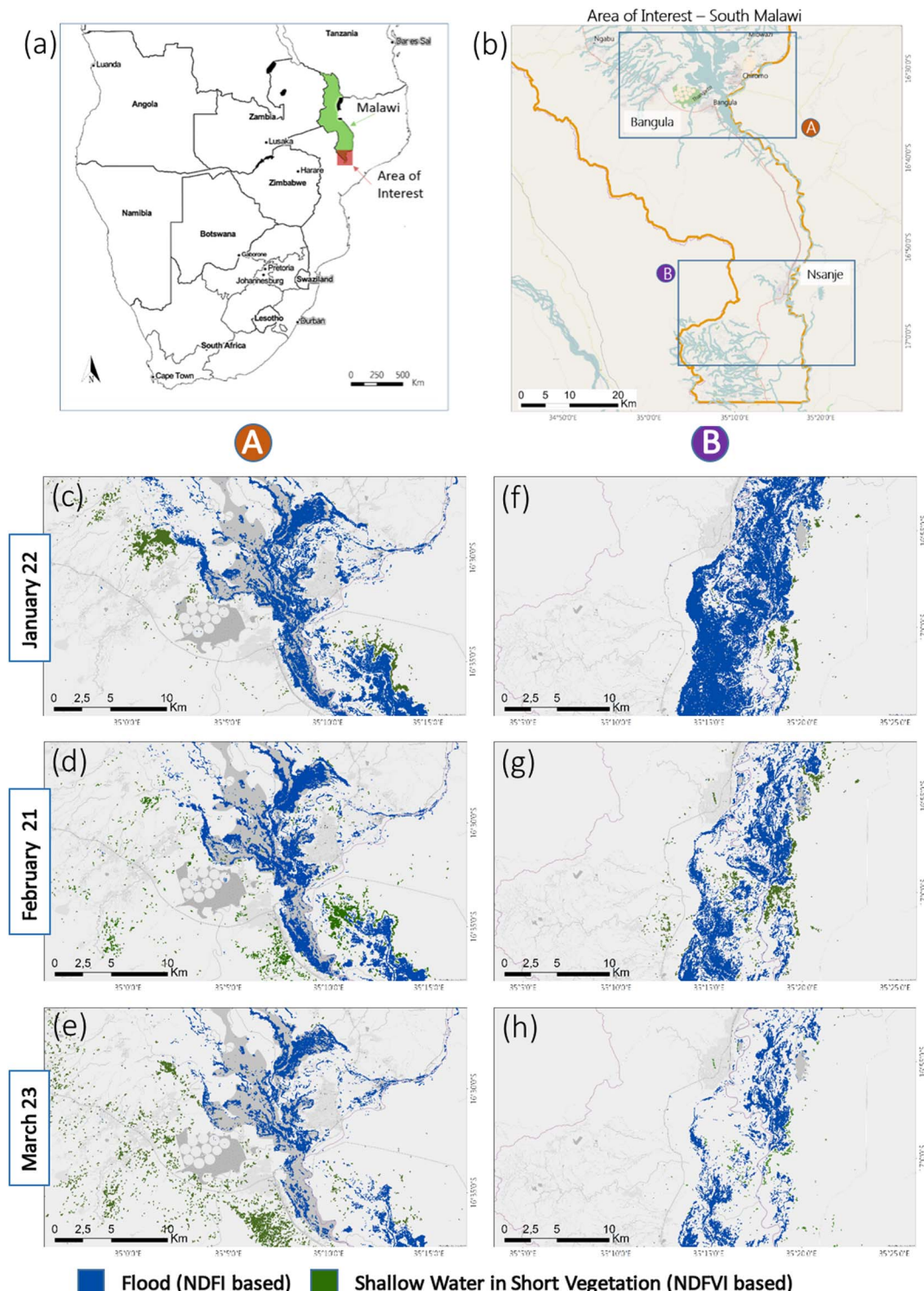


Fig. 4. Malawi Flood 2015, Area of Interest and results. Overview (a) and detail (b) of the area of interest: area (A) refers to the surroundings of Bangula in the Chikwawa district and area (B) refers to the surroundings of Nsanje. Results obtained using Sentinel-1 data for area (A) are reported for January 22 (c), February 21 (d) and March 23 (e); results for area (B) are reported for January 22 (f), February 21 (g) and March 23 (h). Blue areas correspond to flood, green areas to shallow water in short vegetation. (For interpretation of the references to color in this figure legend, the reader is referred to the web version of this article.)

see in Fig. 6(d). In light blue we can see permanent water bodies and in orange bare soils and transitional pixels which fall in the surrounding of water bodies. The same map (Fig. 6) reports also pixels belonging to area 2A, 2B and 2C of the NDFI plane (see Fig. 2), which are barely distinguishable. Out of 5 million flooded pixels appearing in the final flood map, only 20 thousand pixels correspond to area (2A), 0.4% of the total. Pixels belonging to area (2D) are 53 thousand, the 1% of the

overall flooded pixels.

The majority of them falls over bare soil and mountainous regions. They are excluded by filtering steps (morphological, area and slope filtering), which in this case reduce them to 17 thousand. Fig. 6(e) shows pixels belonging to area (3A.1) and (3A.2). These pixels are dropped by the final maps, which make sense in most of the cases except in the proximity of flooded areas where they could be included in

Table 2
Malawi, 2015 dataset.

Sensor (band) imaging mode	Orbit pass rel. orbit num. (pol)	Dates of acquisition	Total N. images
S1 (C) GRDH 10 m	Ascending 101 (VV)	From 17/Nov/2014 To 21/Feb/2015	2 reference 2 flood
S1 (C) GRDH 10 m	Descending 6 (VV)	From 11/11/2014 To 23/03/2015	3 reference 5 flood

the final flood map. The dilation filter partly adjust this possible error, which is nevertheless acceptable. Fig. 6(f) show the resulting analysis for the NDFVI index. Pixels belonging to area (V2A) are barely noticeable in the image. They are < 5% of all the pixels classified as shallow water in short vegetation, making also this error negligible.

3.2. Veneto, Italy 2010

In the morning of November 1, 2010, the city of Vicenza and its province, north-east of Italy, woke up submerged by water. Exceptional rainfall from October 31 to November 2 led to a serious hydraulic stress in the region. Local rainfall accumulation exceeded 500 mm and the average widely surpassed 300 mm. An overall of 262 municipalities in the Veneto region were affected and some badly hit by the flood. The event lasted until mid-November, leading to roughly half billion Euros damage, three fatalities, 3500 displaced and > 500 thousand people

affected (Floris et al., 2012; Scorzini and Frank, 2015). This section analyses three main flooded areas as shown in Fig. 7(a-b): Vicenza and its surrounding (A), Bovolenta area at the south of Padua (B) and Saleto area at the south of Colli Euganei (C).

3.2.1. Data used

The event was observed in different dates and resolutions by several SAR sensors. CSK acquired the first image at 5:30 am of November 1, 2010 right before the first overflow, showing a wet environment with little areas of standing water. At 9:30 am of the same day, ENVISAT-ASAR captured the first outflow at the north and south of Vicenza. On November 2, RS2 acquired the first precise information about the flood extent. Only on November 3, after the activation by the Italian civil protection, CSK was able to acquire the first useful image, after the peak of the flood for the city of Vicenza, but around the peak for the two test areas. CSK acquired one image per day until November 7, allowing the monitoring of the event at high resolution (3 m). Nevertheless, the different geometry of acquisition (due to satellite activation) are not optimal for CD approaches and the high incidence angles make flood mapping more difficult due to the increasing of shadowing and layover effects. TerraSAR-X (TSX) acquired only one image during the event on November 6, with the same incidence angle of the only one available from the archive over the area, dated December 2008, allowing a precise and easy flood mapping. Finally, ASAR provided an image on November 12 monitoring the end of the event. Table 4 summarizes the dataset for the flood in Veneto 2010. Many sensors had to be used to monitor the event with different viewing geometries. Despite many

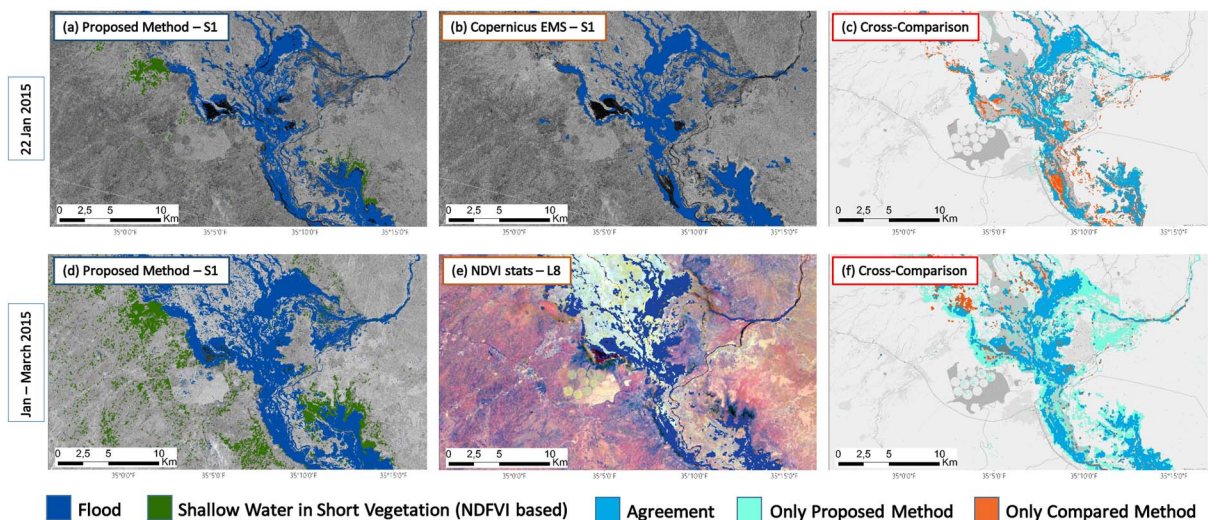


Fig. 5. The images are showing cross-comparison results on the surroundings of the city of Bangula. The top row, shows the results for 22 January 2015: (a) flood map obtained with the proposed method; (b) flood map issued by Copernicus EMS; (c) cross-comparison. The map shows the agreement between the two maps (blue), the flood areas reported only by the proposed method (light blue) and the ones only reported by the compared method (orange). A large cluster of orange pixels can be noted in the central bottom part of the image due to the fact that we did not exclude permanent water bodies using ancillary data. Instead, we used only statistics from the images available during the rainy season. The bottom row shows the results for the period Jan-Mar 2015: (d) flood map obtained with the proposed method; (e) flood map obtained using a threshold on the NDVI statistics (max, mean and min used as RGB combination); (f) cross-comparison. (For interpretation of the references to color in this figure legend, the reader is referred to the web version of this article.)

Table 3

Line 1): January 22nd 2015 cross-comparison between NDFI based map and Copernicus EMS product. Line 2): cross-comparison between NDFI-based and NDVI-based flood map for the period January–March. The area covered by the three different products is different therefore also the area of overlap.

Cross-comparison results						
Compared methods		Date	Agreement	Only method 1	Only method 2	
Method 1	Method 2					
1) 2)	Proposed method (S1 data) Proposed method (S1 data)	Copernicus EMS (S1 data) NDVI-based method (L8 data)	22/Jan/2015 Jan–March/2010	71.6 km ² 449 km ²	37.1 km ² 546 km ²	22.9 km ² 79.6 km ²

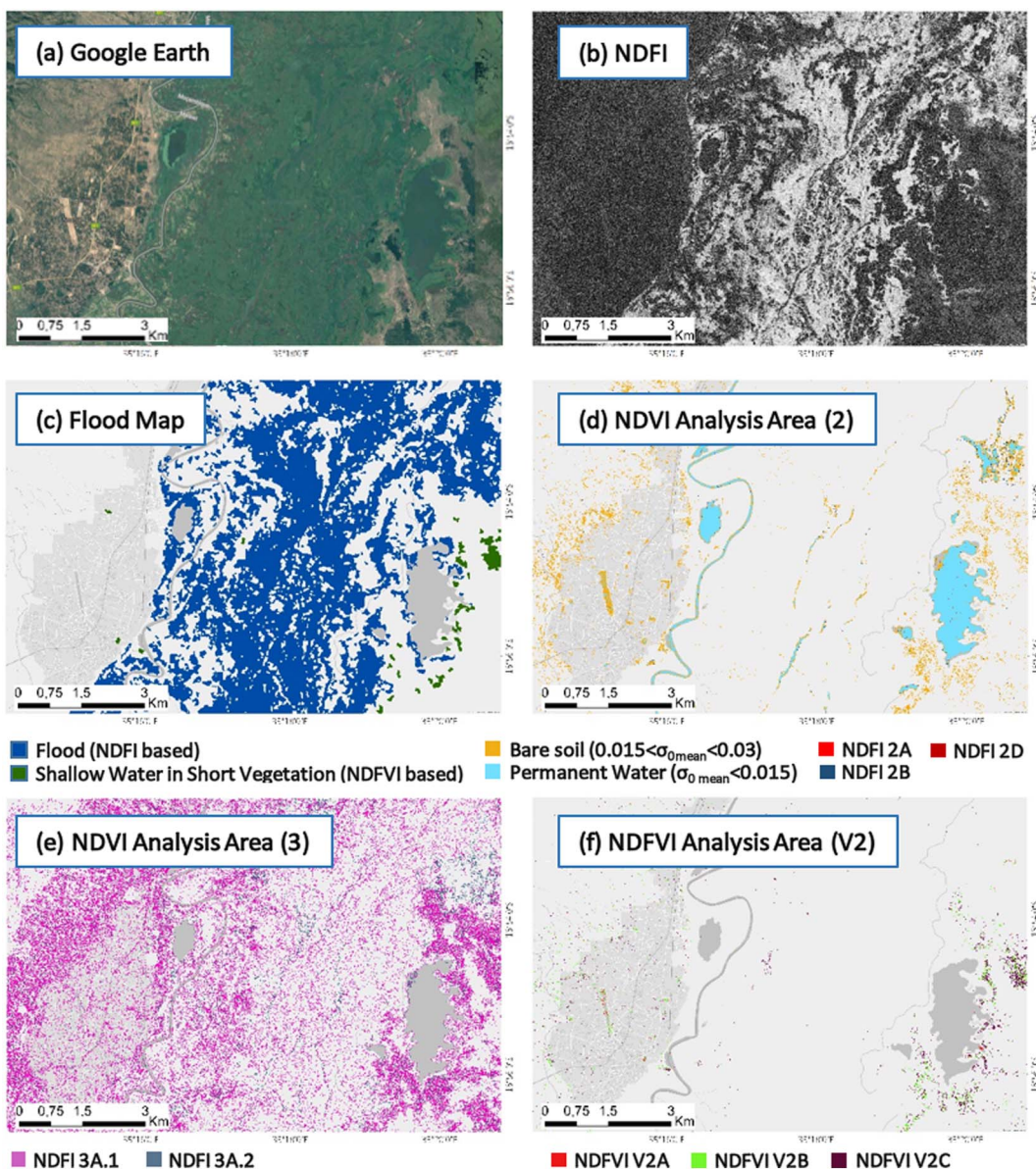


Fig. 6. Index analysis in the surrounding of the city of Nsanje. (a): Google Earth image of the area of study. (b): NDFI image. NDFI value goes from 0 (black pixels) to 1 (white pixels). Flooded areas (bright pixels) are easily recognizable. (c): flood map showing also shallow water in short vegetation based on the NDFVI index. (d): Analysis of the area (2) of the NDFI plot (see Fig. 2). Very few pixels belong to areas (2A) and (2D), which in fact are not visible on the map, showing that these errors are negligible. (e): Analysis of the area (3A) of the NDFI plot (see Fig. 2). (f): Analysis of the area (VA) of the NDFVI plot (see Fig. 3). We can barely see red pixels belonging to area (V2A) showing that this source of error is negligible. (For interpretation of the references to color in this figure legend, the reader is referred to the web version of this article.)

years of operation, the amount of reference images covering the study area was very limited. ESA data were freely downloaded from the internet via the ESA EOLi portal (ESA EOLi, European Space Agency, Earth Observation Link, n.d), while TSX, RS2 and CSK were kindly provided respectively by the German Aerospace Center, the Canadian Space Agency and the Italian Space Agency.

Moreover, the 2012 DEM of the Italian ministry of Environment available at 1 m spatial resolution has been used to filter steep areas.

3.2.2. Results

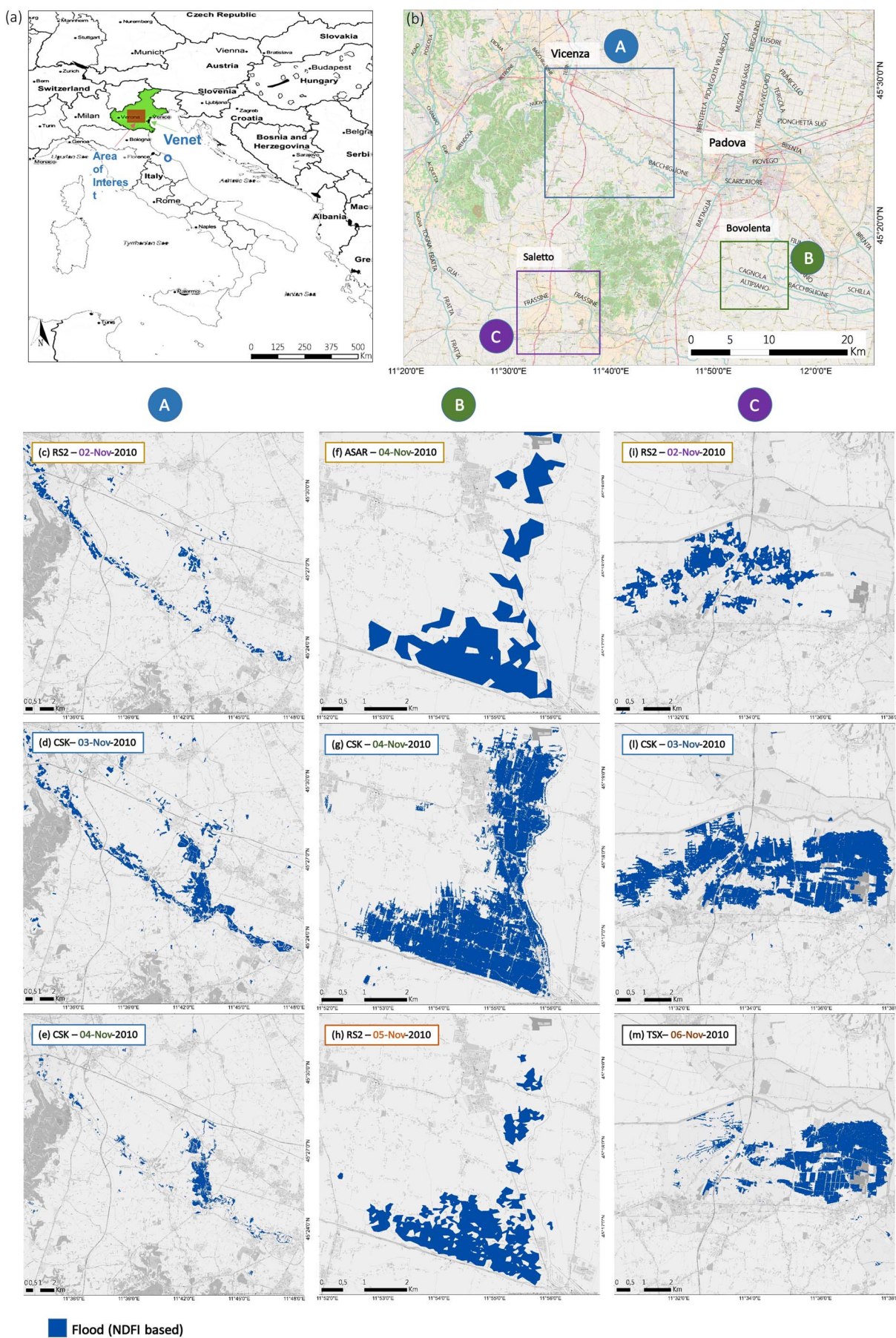
A total of 11 flood maps were produced for this flood event at different resolutions, precisions and coverages. CSK and TSX acquire at very high resolution (3 m), whereas RS2 and ASAR at lower resolution (25 m and 150 m respectively).

Part of these results are reported in Fig. 7. Column A in Fig. 7 shows the maps derived for the area of Vicenza on November 2 using RS2 (Fig. 7c), on November 3 and 4 using CSK (Fig. 7d,e). Column B in

Fig. 7 shows the maps of Bovolenta on November 4 using ASAR (Fig. 7f), on November 4 using CSK (Fig. 7g) and on November 5 using RS2 (Fig. 7h). Column C in Fig. 7 shows the maps of Saleto on November 2 using RS2 (Fig. 7i), on November 3 using CSK (Fig. 7l) and on November 6 using TSX (Fig. 7m). From these maps we can appreciate the evolution of the event and the different resolution of the products.

The International Center on Environmental Monitoring foundation (CIMA) produced the same maps for the Italian Civil Protection during the event in 2010 with a method based on automatic thresholding and region growing, presented in detail in Pulvirenti et al. (2014). CIMA did not provide any accuracy figure of these maps since they were not validated with field measurements.

The results obtained with the proposed method for November 3 (Fig. 8(a)) and November 6 (Fig. 8(d)), were cross-compared with the maps produced by CIMA foundation for the same dates, respectively Fig. 8(b) and (e). The cross-comparison for the area of Vicenza is shown in Fig. 8(c) and for the area of Bovolenta in Fig. 8(f). Fig. 8(i) shows the



(caption on next page)

Fig. 7. Flood in Veneto 2010, area of interest and results. Overview (a) and detail (b) of the areas of interest. Columns A (c–e) shows the results over the surroundings of the city of Vicenza; column B (f–h) the results over the surroundings of the town of Bovolenta at the south of Padova; column C (i–m) the results on the surroundings of the town of Saleto. Results are reported for different sensors (RS2, ASAR, CSK and TSX) and for different dates (from November 2, 2010 to November 6, 2010) as indicated by the label in each image.

cross-comparison between the results obtained for November 6 with the proposed method using CSK data (Fig. 8(g)), and TSX data (Fig. 8(h)). The results show very good agreement (blue), with areas reported as flooded only by the proposed method (light blue). Very few pixels are reported only by CIMA foundation (orange). Table 5 confirms the high agreement between the two products but also shows how the proposed methods is reporting a wider flooded area. This is partly explained by analyzing Fig. 8(c), (f) and (i), which show how the proposed method is capturing flooded areas not reported by CIMA's products.

The different geometries of acquisition create different shadowing and layover effects which result in false alarms. Despite the sub-optimal datasets, the proposed method is able to produce very detailed maps. Using the maps produced by CIMA foundation for comparison, the specific agreement on flooded areas is on average 87% for the 5 maps and the overall agreement is 96.5%.

3.3. Northern Uganda, 2015

Forecast-based Financing (FbF) project of the International Federation of the Red Cross and Red Crescent Climate Centre consists of a series of preparedness actions to take to reduce the impact of possible flood events. Actions start after the triggering of a warning system. The warning system is based on the river discharge forecasts produced by the Global Flood Awareness System (GloFAS). Uganda Red Cross successfully initiated actions for the first time in November 2015 following a forecast that triggered the warning system and used the Preparedness

Fund provided by the project (Coughlan De Perez et al., 2015).

To validate the triggering of actions in the Teso region of North Eastern Uganda, Fig. 9(a) and (b), several maps were produced using S1 data and the method proposed in this paper.

The region analyzed is swampy and prone to flood during the two rainy seasons of May and October.

3.3.1. Data used

The systematic acquisition over Uganda since the beginning of the S1 mission resulted in a total of 26 reference images in one year as shown in Table 6. Compared to the pre-S1 scenario, such as the one in Veneto explained in Section 3.2, this is a big change. The method presented is designed specifically to deal with such big amount of data and exploiting cloud computing. To process this big amount of data (29 S1 images) we used Google Earth Engine (GEE), which at the time of our analysis had just ingested the S1 catalog. GEE allowed us to process the data and retrieve the results in few minutes. The SRTM DEM has been used to filter steep areas.

3.3.2. Results

The maps were produced for the Red Cross/Red Crescent Climate Centre in order to understand whether a real flood occurred in the area where their emergency warning system was triggered. The bimodal rainy season of the study area leads to a frequent change in the land cover, which made difficult the interpretation of the statistics given that no ground truth was available. Despite the difficulties, the statistics we

Table 4

Veneto 2010 Dataset. CSK data with the same incidence angle is highlighted. Despite many years of operation, older SAR missions have few reference images in their archive.

Sensor (Band) Imaging Mode (Res.)	Orbit (Pol)	Date	Incidence Angle	Status	Total N. Images
COSMO-SkyMed (X)	Descending (HH)	31/Nov/2008	27.7-30.8	Reference	2 Ref.
		28/Apr/2010	28.9-31.8	Reference	3 Flood
	03/Nov/2010	37.4-40.1	Flood		
		04/Nov/2010	40.1-42.6	Flood	
	Stripmap (3m)	06/Nov/2010	27.7-30.9	Flood	
	Ascending (HH)	29/Aug/2010	31.1-34.2	Reference	1 Ref.
		01/Nov/2010	31.1-34.2	Flood	2 Flood
		07/Nov/2010	47.0-49.2	Flood	
TerraSAR-X (X)	Ascending	24/Dec/2008	31.3	Reference	1 Ref.
Stripmap (3m)	(HH)	06/Nov/2010	31.5	Flood	1 Flood
Radarsat-2 (C) ScanSAR (25m)	Descending (HH)	11/Feb/2010	30.33	Reference	1 Ref.
		02/Nov/2010	30.28	Flood	1 Flood
	Ascending (HH)	18/Sep/2010	30.17	Reference	1 Ref.
		05/Nov/2010	30.3	Flood	1 Flood
ENVISAT-ASAR (C)	Ascending (VV)	06/Sep/2010		Reference	1 Ref.
		06/Nov/2010		Flood	1 Flood
	Descending (VV)	19/Sep/2010		Reference	2 Ref.
		11/Oct/2010		Reference	1 Flood
WideSwath (150m)		12/Nov/2010		Flood	
		01/Nov/2010		Reference	1 Ref.
	(HH)	04/Nov/2010		Flood	1 Flood

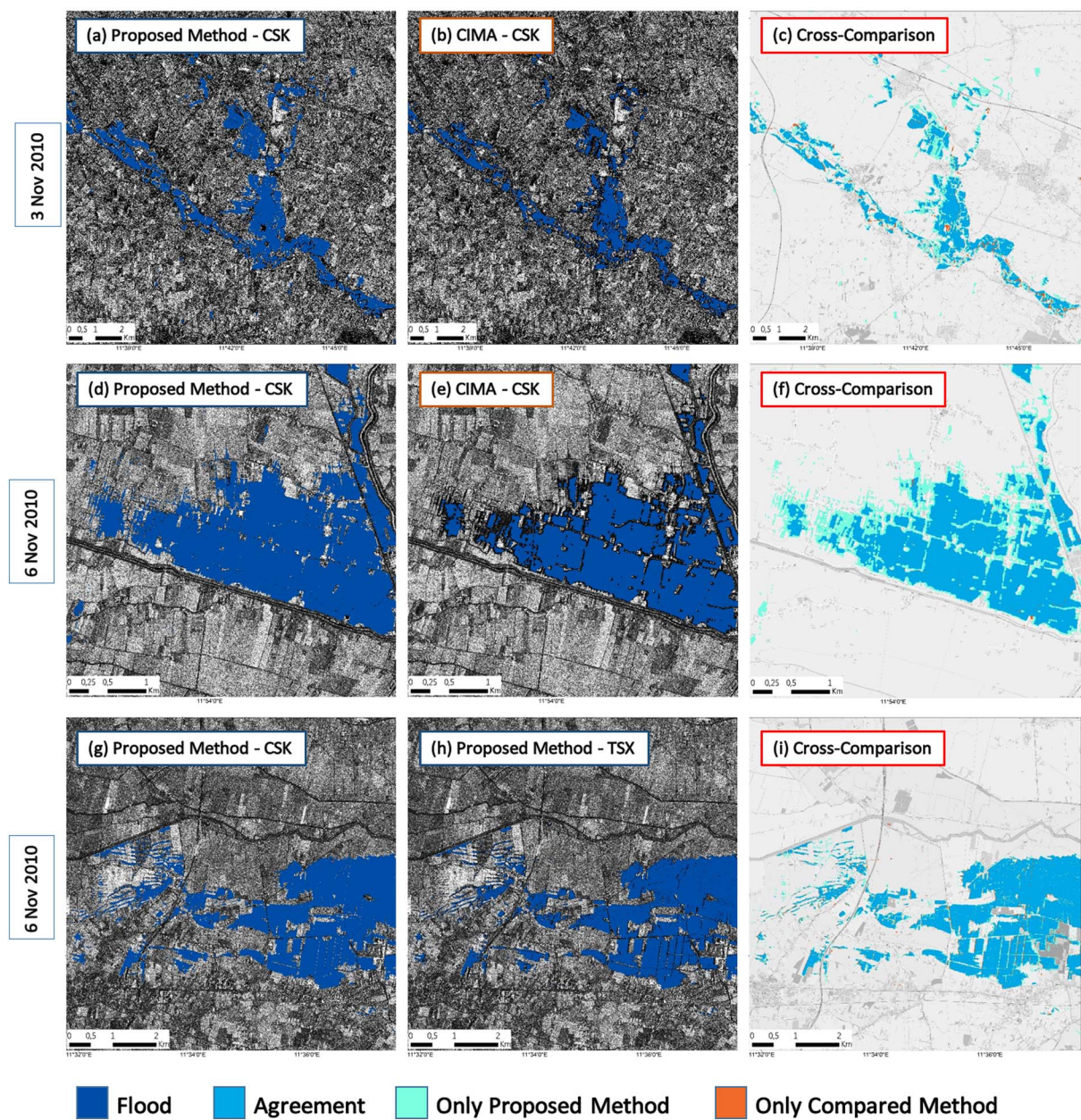


Fig. 8. Results of the cross-comparison using different SAR data and methods. Cross-comparison of the results obtained with the proposed method, (a) and (d), and the ones obtained by CIMA foundation (b) and (e) for Vicenza (c) and Bovolenta (f) for the dates indicated in each row. Cross-comparison of the results obtained with the proposed method using CSK data (g) and TSX data (h) is shown in (i). In the results of the cross-comparison agreement is shown in blue, flooded areas reported only by the proposed method in light blue and flooded areas reported only by the compared method in orange. (For interpretation of the references to color in this figure legend, the reader is referred to the web version of this article.)

Table 5

Cross-comparison of the flood maps obtained with the proposed method for Veneto 2010 case study. Line 1) and 2) show the comparison between the results obtained with the proposed method and the ones obtained by CIMA foundation using the same data (CSK and TSX respectively). Line 3) shows the comparison between the results obtained for November 6, 2010 with the proposed method using CSK and TSX data.

Cross-comparison results					
Compared methods		Date	Agreement	Only method 1	Only method 2
Method 1	Method 2				
1) Proposed method CSK data	CIMA	03/Nov/2010 06/Nov/2010 07/Nov/2010	20.8 km ² 9.7 km ² 3.6 km ²	12.1 km ² 5.6 km ² 5.6 km ²	1.9 km ² 1.3 km ² 1.3 km ²
2) Proposed method TSX data	CIMA	06/Nov/2010	6.3 km ²	2.7 km ²	1.3 km ²
3) Proposed method CSK data	Proposed method TSX data	06/Nov/2010	8.6 km ²	2.1 km ²	0.5 km ²

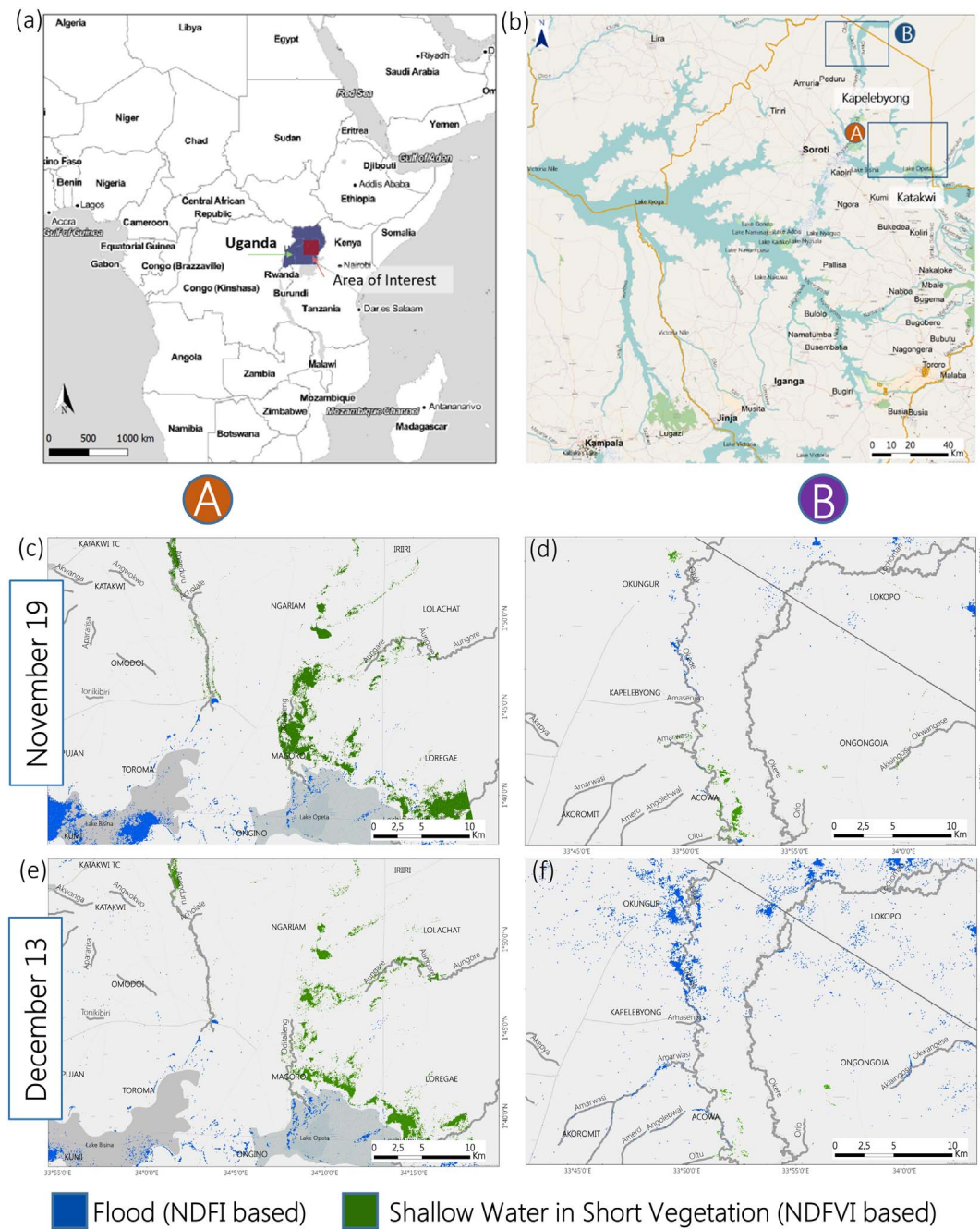


Fig. 9. Uganda Flood 2015, area of interest and results. Overview (a) and detail (b) of the area of interest. Column A, (c) and (e), show the results for the Katakwi region and Column B, (d) and (f), for the Kapelebyong region, on November 19 and December 13 as indicated by the labels.

Table 6
Uganda 2015 dataset.

Sensor (band)	Orbit pass	Date of acquisition	Total N. images
Imaging mode	Rel. orbit num. (pol)		
S1 (C)	Ascending	From 19/Oct/2014	16 reference
GRDH 20 m	28–29 (VV)	To 13/Dec/2015	2 flood
S1 (C)	Descending	From 26/Nov/2014	10 reference
GRDH 20 m	50 (VV)	To 09/Nov/2015	1 flood

computed were based on a long time-series and allowed us to produce three maps where the NDFVI identified shallow water in short vegetation. Fig. 9(c) and (e) show the results for the Katakwi district (column A), while Fig. 9(d) and (f) for the Kapelebyong district (column

B) for November 19 and December 13, 2015. We can observe that in the Katakwi region, part of the lake on the west side of the map is reported as flooded. This is due to the fact that the lake was unusually dry during the period October 2014 to October 2015. The statistics on the reference stack accurately reported that the lake was dry. The rainfall events that occurred in November were unusual and created an anomaly in the water surface of the lake which is considered as flooded.

Fig. 10 zooms on a small area of the Kapelebyong district Fig. 10(a). Fig. 10(b) shows the flood map for this area where shallow water in short vegetation were detected. Fig. 10(c) shows a very low mean value of the backscattering prior to the flood event. In comparison, the backscattering has increased in November 19 (flood event date) as captured by the high values of NDFVI in Fig. 10(d). This allowed the detection of shallow water in short vegetation.

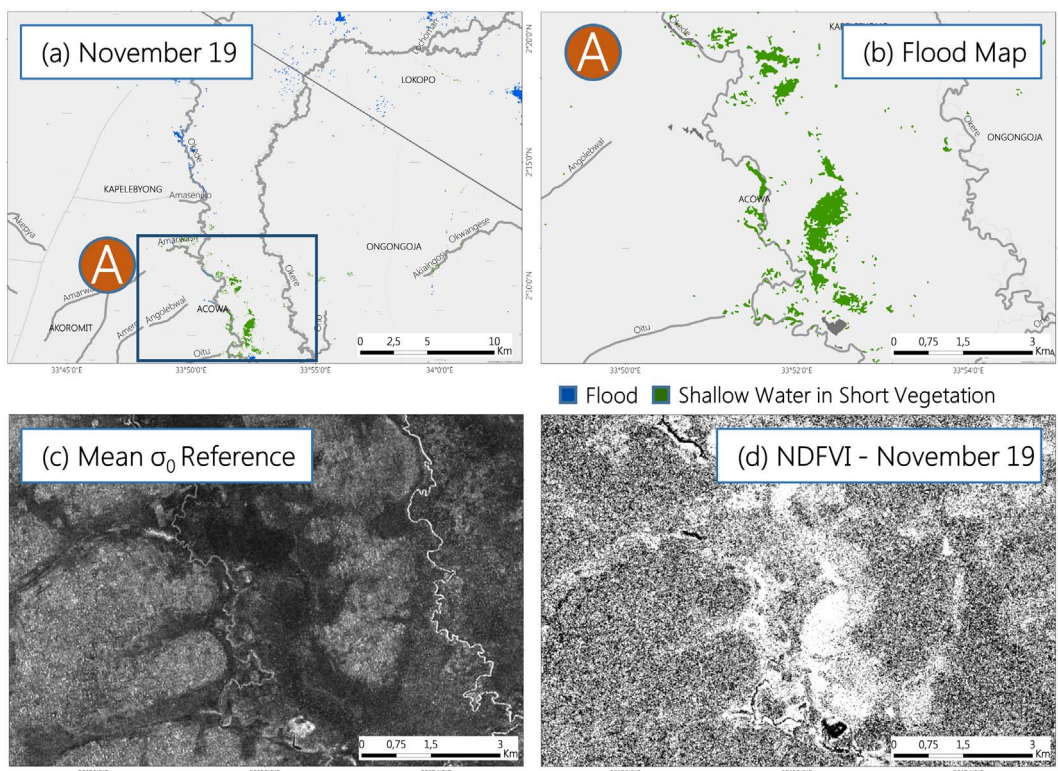


Fig. 10. Detail of the Kapelebyong result on November 19. (a): location of the area of interest. (b): detail of the result. We can note shallow water in short vegetation. (c): σ_0 mean image. We can note the dark pixels in the area that was later reported as shallow water in short vegetation. (d): NDFVI value. We can see how the index highlights areas that experienced an increase of backscattering due to shallow water in short vegetation.

3.4. Additional filtering to refine the flood map

We showed in the Section 2.5 how the threshold on the NDFI could result in the inclusion of some non-flooded pixels in the final flood map (i.e., areas 2A and 2D of the NDFI plot in Fig. 2(b) and (c)). These errors proved to be negligible in the cases where we tested the method; nevertheless, further filtering could improve the quality of the map in case of need. To this purpose, after converting the raster flood map into polygons, for each of them one can compute the mean and standard deviation of the corresponding $\sigma_{0\min}$ and $\sigma_{0\text{mean}}$. Then, polygons with mean ($\sigma_{0\text{mean}}$) < 0.015 (area 2A in the NDFI plot) shall be filtered out together with polygons with mean ($\sigma_{0\min}$) > 0.03 (area 2D in the NDFI plot). This step was not necessary in the cases of Malawi and Uganda given the good quality of the dataset; nonetheless, for a sub-optimal datasets (e.g., characterized by a short reference time-series and/or the presence of images with different geometry of acquisition), these additional filtering steps are recommended. Furthermore, in these cases false alarms could also occur due to the different shadowing or layover effect in the different images of the series or due to changes in the land cover that may occur between the first reference image and the flood image. Fig. 12 reports an example for the 2010 Veneto flood where a new construction caused a false alarm. Specifically, Fig. 12(a) shows brighter tones in the middle due to the high backscattering caused by double-bounce on the building under construction. The decrease of backscattering in Fig. 12(b) is due to the shadow by the completed building and not the presence of water. In this case, a filter in the $\sigma_{0\text{mean}}$ standard deviation (which is relatively high for the corresponding polygon) allows to easily identify the false alarm (Fig. 12(c)).

Backscatter standard deviation inside flooded polygons can be useful to detect false alarms which generally present very high values either in the reference or in the flood images. Based on several experiments, a threshold of 2 (in the reference or in the flood image) for the standard deviation proved a rather effective choice for detecting misclassified areas.

4. Discussion

The new method we proposed aim at exploiting new big EO data. It is especially designed for using S1 data. A statistical analysis on a large amount of reference images gives more precise information about pre-event conditions and allows a much more robust and precise detection of changes when a flood occurs. This was shown by the three case studies presented, in particular for Malawi and Uganda where S1 data were used. For these two cases, it was also possible to detect shallow water in short vegetation, an information that is currently not reported by emergency mapping centers despite of a high demand for economic impact assessment.

The Malawi dataset, the first flood captured by S1, was not ideal since S1 was at its initial operational phase and few archive images were available. However, despite the short time-series, we obtained precise results, similar to the Copernicus EMS product. The main difference between the two approaches consists in the way permanent water bodies are considered. In particular, Copernicus EMS excluded them using ancillary data; whereas in our case, permanent or semi-permanent water bodies were excluded from the map only if they appeared in the statistics of the reference images. This is an important difference since several floodplain are used for agriculture during drier seasons. Avoiding to report these areas as flooded could affect the estimation of economic impact in a post-disaster assessment or the emergency operations planning and management. Vice versa, our maps did not report certain areas with low backscattering reported by Copernicus EMS. Our method excluded them because they had low backscattering also in the reference statistics. This shows the power of CD algorithms in comparison to others based on single image thresholding. It also shows the power of the frequent acquisitions of these new satellites, which can improve CD methods, such as the one proposed by Long et al. (2014), providing more robust reference information.

Even though flood indices have been developed having in mind EO big data, the proposed method was tested on a typical pre-S1 case

study, i.e. a scenario with few acquisitions and almost no archive data useful for CD. For the Veneto flood of 2010, we tested the method with 4 different sensors at different resolutions: CSK and TSX at 3 m, RS2 at 25 m and ASAR at 150 m. We also had the chance to test it for HH polarization as in the case of ASAR and RS2. The method showed to be robust since the identical processing steps were followed obtaining in all the cases very good results. Moreover, the threshold value on the NDFI was the same for each dataset (i.e. 0.7). The method performs well also at lower resolutions. Given the limited fluctuation of SAR backscattering at these resolutions, the final flood maps presented less spurious clusters.

The comparison of CKS- and TSX-based products shows very little differences, indicating the robustness of the proposed method, which gives the same performances using data coming from different sensors. In this case, the main difference is due to different time of acquisition and different quality in the original data.

The comparison with the maps produced by CIMA foundation for the Italian Civil Protection, shows very good agreement and highlights how the proposed method provides more detailed maps, Fig. 8(c) and (f). CIMA's maps are produced based on the method presented in Pulvirenti et al. (2014), which uses filtering after the thresholding. This method is not based on CD and in fact commits errors in reporting permanent water bodies, which are often marked as flooded areas.

Despite the very good cross-comparison qualitative assessment, it is worth pointing out that the considered maps have not been validated with in-situ surveys. In particular, to our knowledge no field measurements were available for any of the investigated case studies. This is a key limitation not only of this work, but of the flood mapping literature in general, where most of the methods presented are applied without any ground truth information for quantitative assessment.

Our proposed method is not strongly user-dependent. In fact, the same thresholding value has been used in all cases as well as the filtering steps. This is a strong point since many methodologies are based on the choice of many parameters to obtain the final map, such as is the case of Martinis et al. (2015) or Long et al. (2014), where the optimal threshold value is decided by the analyst. An interesting example to find optimal threshold values and reduce user dependence was proposed by Manjusree et al. (2012). The method is presented only for a sensor and not in different environments. Our proposed method instead shows to work with different sensors and in different ecosystems. Moreover, the filtering steps proposed in our method are based on physical reasoning, slope and dimension of spurious clusters. Therefore, the influence of the analyst on the final result is limited.

Regarding shallow water in short vegetation, we did not have the chance to compare our results with others, since, in our knowledge, there was no emergency service reporting this information. In the case of Uganda, radar backscatter during the days when the alerting system was triggered (November 19, 2015) showed a strong increase compared with the mean value in the reference statistics. The increase, very well captured by the NDFVI index, Fig. 10(d), was not comparable with a

simple change in vegetation. The mean σ_0 over flooded areas increased on average of about 2.5 dB, to an average value of -5 dB. The information that came from the field from the Red Cross indicated that the majority of the reported flood was exactly of this kind as shown in Fig. 11.

In the case of Malawi, shallow water in short vegetation appeared in proximity of zones of "normal" flooding, where they are more likely to happen and where we were expecting them. With the receding of the flood, a larger area of shallow water in short vegetation was detected, which was expected given that the increase of backscattering happens when vegetation starts to emerge from water (Fig. 4(c-h)). This suggests that the results are accurate even though in the future it would be important to validate these products with field measurements. The comparison with L8-based flood maps (Fig. 5) showed interesting results. Despite the usual limitations of cloud coverage for optical sensors, the coupling of this with the method proposed can be of great potential. In fact, thanks to the available cloud computing capacity, the big amount of L8 and S1 images can be quickly processed and additional information about the flood can be provided since acquisitions may come in different days.

The proposed method is simple, robust and transferable. In the near future, it may become suitable for emergency mapping even though a big amount of data is required to be processed. In fact, it has been developed having in mind cloud computing. New services, such as GEE, allowed us to access easily and quickly all the archived Landsat and Sentinel images without the need for downloading them. Data were processed in the cloud in a very short amount of time. For instance, in the case of Uganda it took us few minutes to process and export the final flood map from GEE. In between, there is the time needed to explore the data and study the case, but this time is in common with all the available methods. The limitation could be the availability of new acquisitions, which might be uploaded with some delay in the cloud. Nevertheless, this limitation can be easily overcome by uploading manually the event image in the GEE, slightly slowing down the process, but still allowing a rapid mapping in a time comparable with other operative methods, such as the ones proposed by Martinis et al. (2015) and Pulvirenti et al. (2014).

5. Conclusion

A new method based on time-series statistical analysis is proposed for flood mapping with the aim of exploiting the big EO data coming from the new Sentinel 1 constellation. Two indices are proposed for mapping flooded areas: the Normalized Difference Flood Index (NDFI), for mapping open water and the Normalized Difference Flood in Vegetation Index (NDFVI) for mapping shallow water in short vegetation. We propose a temporal statistical analysis to capture the normal condition of the land cover of the area (mean pixel values in the reference images) and the discontinuity produced by the presence of flood water (minimum and maximum pixel values in the stack also

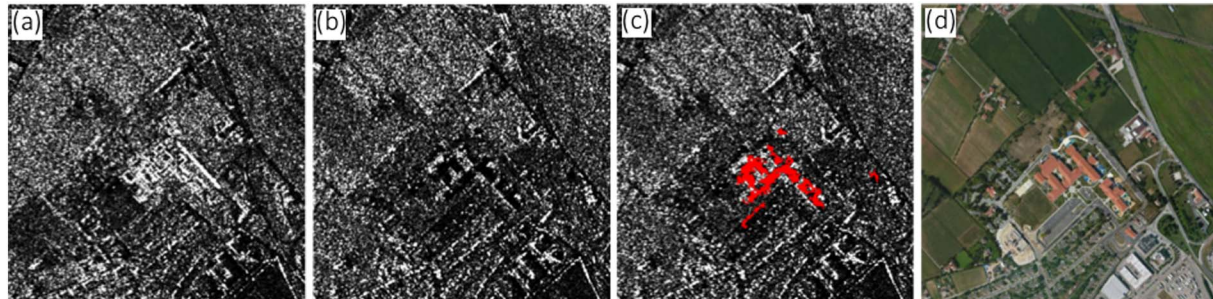


Fig. 11. Example of false alarm due to a construction of a new building. (a) CSK reference image acquire in 2008 with a building in construction. The short elevation of the building gives high backscattering and almost no shadow. (b) CSK image acquired during the 2010 flood with the same building completed, which now creates a shadow. (c) result after the threshold on the NDFVI shows the roof shadow as flood (d) Google Earth image of the same area for comparison.



Fig. 12. Images shot by the Red Cross in Kapelebyong area right after the triggering of the alert (November 13, 2015) showing the kind of flooding that hit the area.
<https://www.flickr.com/photos/climatecentre/albums/72157660532090507/with/23066963062/>

containing the images of the flood). The use of normalized indices built on statistics has the aim of compressing the information of long time-series (EO big data). A threshold is applied to the two indices to derive the flood maps. The value of the thresholds remain constant independently from the sensors used, the resolution and the environment analyzed. Additional filtering steps are performed to improve the accuracy of the map.

The proposed methodology exhibits the following advantages: i) it is non-user dependent; ii) it can be easily automated; iii) it is robust since the same workflow (in particular the same threshold values) is applied to different floods in different environments and using different SAR sensors, polarizations and resolutions; iv) the use of time-series improves the robustness of the reference image allowing a more precise mapping; and v) it reports shallow water in short vegetation, a product usually non reported by emergency management services.

Given the robustness and accuracy showed in all the investigated cases, the method looks suitable for operational mapping in the near future. The advent of new cloud computing capability and the availability of satellite data in the cloud, such in the case of GEE, allow a fast analysis and export of the results.

Nevertheless there are still some limitations. The use of old SAR data prior to 2014, which usually are sparse and acquired with different geometries, showed to be more complicated and required more filtering steps even though precise results were obtained.

In urban areas we could not obtain good results. The resolution of S1 did not allow for detecting changes using only radar intensity and at the moment of this analysis no Single Look Complex data were available on the areas considered in this paper and it remains a possibility for further improvement. CSK could have the potential for showing changes in urban areas but for the flood analyzed in this work the dataset did not allow the detection of floods because the images were acquired with different geometries and therefore the different radar shadow over urban areas did not allow the detection of water.

Abbreviations

CD	Change Detection
Copernicus EMS	Copernicus Emergency Management Service
CSK	COSMO-SkyMED
[dB]	decibel
DLR	German Aerospace Center
EM	Emergency Management
EO	Earth Observation
ESA	European Space Agency
GEE	Google Earth Engine
GRDH	Ground Range Detected High resolution
L8	Landsat-8
NDVI	Normalized Difference Vegetation Index
NDFI	Normalized Difference Flood Index

NDFVI	Normalized Difference Flood in Vegetation Index
SAR	Synthetic Aperture Radar
RS2	Radarsat-2
S1	Sentinel-1
TSX	TerraSAR-X

Acknowledgments

The authors thank the Italian Space Agency that provided COSMO-SkyMED data through e-GEOS, the German Aerospace Center for the TerraSAR-X data, the European Space Agency for the ASAR and Radarsat-2 data and CIMA foundation for the maps used in the validation steps. Moreover, the authors thank the two anonymous Reviewers and the RSE editorial staff for the comments and suggestions that helped improving substantially this work.

References

Alsdorf, D.E., Rodriguez, E., Lettenmaier, D.P., 2007. Measuring surface water from space. *Rev. Geophys.* 45 (2), 1–24. <http://dx.doi.org/10.1029/2006RG000197.1>. INTRODUCTION.

Arnesen, A.S., Silva, T.S.F., Hess, L.L., Novo, E.M.L.M., Rudorff, C.M., Chapman, B.D., McDonald, K.C., 2013. Monitoring flood extent in the lower Amazon River floodplain using ALOS/PALSAR ScanSAR images. *Remote Sens. Environ.* 130, 51–61. <http://dx.doi.org/10.1016/j.rse.2012.10.035>.

Atlas, D., Moore, R.K., 1987. The measurement of precipitation with synthetic aperture radar. *J. Atmos. Ocean. Technol.* 4 (3), 368–376. [http://dx.doi.org/10.1175/1520-0426\(1987\)004<0368:TMOPWS>2.0.CO;2](http://dx.doi.org/10.1175/1520-0426(1987)004<0368:TMOPWS>2.0.CO;2).

Bazi, Y., Bruzzone, L., Melgani, F., 2005. An unsupervised approach based on the generalized Gaussian model to automatic change detection in multitemporal SAR images. *IEEE Trans. Geosci. Remote Sens.* 43 (4), 874–887. <http://dx.doi.org/10.1109/TGRS.2004.842441>.

Bessis, J.L., Bequignon, J., Mahmood, A., 2004. Three typical examples of activation of the international charter “space and major disasters”. *Adv. Space Res.* 33 (3), 244–248. [http://dx.doi.org/10.1016/S0273-1177\(03\)00467-8](http://dx.doi.org/10.1016/S0273-1177(03)00467-8).

Bragg, W., 1913. The diffraction of short electromagnetic waves by a crystal. *Proc. Camb. Philos. Soc.* 17, 43–57. <http://dx.doi.org/10.1017/S0567739472000609>.

Brisco, B., Schmitt, A., Murnaghan, K., Kaya, S., Roth, A., 2011. SAR polarimetric change detection for flooded vegetation. *Int. J. Digital Earth* 6 (July 2014), 1–12. <http://dx.doi.org/10.1080/17538947.2011.608813>.

Brivio, P.A., Colombo, R., Maggi, M., Tomasoni, R., 2002. Integration of remote sensing data and GIS for accurate mapping of flooded areas. *Int. J. Remote Sens.* 233 (3), 143–161. <http://dx.doi.org/10.1080/01431160010014729>.

Ciappa, A., Grandoni, D., Nicolosi, P.A.S., Cannizzaro, V.A.S., Piana, S.P., 2015. Use of cosmo-skymed data for innovative and operational applications. 1, 215–218.

Copernicus EMS, Copernicus Emergency Management Service <http://emergency.copernicus.eu/mapping/copernicus-emergency-management-service>.

Cossu, R., Schoepfer, E., Bally, P., Fusco, L., 2009. Near real-time SAR-based processing to support flood monitoring. *J. Real-Time Image Proc.* 4 (3), 205–218. <http://dx.doi.org/10.1007/s11554-009-0114-4>.

Coughlan De Perez, E., Van Den Hurk, B., Van Aalst, M.K., Jongman, B., Klose, T., Suarez, P., 2015. Forecast-based financing: an approach for catalyzing humanitarian action based on extreme weather and climate forecasts. *Nat. Hazards Earth Syst. Sci.* 15 (4), 895–904. <http://dx.doi.org/10.5194/nhess-15-895-2015>.

Danklmayer, A., Chandra, M., 2009a. Precipitation effects for Ka-band SAR. In: *Proc. of Advanced RF Sensors For Earth Observation (ARSI)*. 1. pp. 1368–1370.

Danklmayer, A., Chandra, M., 2009b. Precipitation induced signatures in SAR images. In: European Conference on Antennas and Propagation (EuCAP) 2009, EuCAP 2009, 3rd ed. pp. 3433–3437. Retrieved from. http://ieeexplore.ieee.org/xpls/abs_all.jsp?arnumber=5290500

arnumber=5068334.

de Moel, H., Jongman, B., Kreibich, H., Merz, B., Penning-Rowsell, E., Ward, P.J., 2015. Flood risk assessments at different spatial scales. *Mitig. Adapt. Strateg. Glob. Chang.* 20 (6), 865–890. <http://dx.doi.org/10.1007/s11027-015-9654-z>.

Dellepiane, S.G., Angiati, E., 2012. A new method for cross-normalization and multi-temporal visualization of SAR images for the detection of flooded areas. *IEEE Trans. Geosci. Remote Sens.* 50 (7 PART 2), 2765–2779. <http://dx.doi.org/10.1109/TGRS.2011.2174999>.

Dellepiane, S., Bo, G., Monni, S., Buck, C., 2000. SAR images and interferometric coherence for flood monitoring. In: IGARSS 2000. IEEE 2000 International Geoscience and Remote Sensing Symposium. Taking the Pulse of the Planet: The Role of Remote Sensing in Managing the Environment. Proceedings (Cat. No.00CH37120). vol. 6. pp. 2608–2610. <http://dx.doi.org/10.1109/IGARSS.2000.859656>.

Di Baldassarre, G., Schumann, G., Brandimarte, L., Bates, P., 2011. Timely low resolution SAR imagery to support floodplain modelling: a case study review. *Surv. Geophys.* 32 (3), 255–269. <https://doi.org/10.1007/s10712-011-9111-9>.

ESA EO/LI, European Space Agency, Earth Observation Link <https://earth.esa.int/web/guest/eoli>.

Floris, M., D'Alpaos, A., De Agostini, A., Stevan, G., Tessari, G., Genevois, R., 2012. A process-based model for the definition of hydrological alert systems in landslide risk mitigation. *Nat. Hazards Earth Syst. Sci.* 12, 3343–3357. <http://dx.doi.org/10.5194/nhess-12-3343-2012>.

Franceschetti, G., Lanari, R., 1999. *Synthetic Aperture Radar Processing*. CRC press.

Franceschetti, G., Iodice, A., Riccio, D., 2002. A canonical problem in electromagnetic backscattering from buildings. *IEEE Trans. Geosci. Remote Sens.* 40 (8), 1787–1801. <http://dx.doi.org/10.1109/TGRS.2002.802459>.

Giustarini, L., Hostache, R., Matgen, P., Schumann, G.J., Bates, P.D., Mason, D.C., 2013. A change detection approach to flood mapping in urban areas using TerraSAR-X. *IEEE Trans. Geosci. Remote Sens.* 51 (4), 2417–2430. <http://dx.doi.org/10.1109/TGRS.2012.2210901>.

Giustarini, L., Hostache, R., Kavetski, D., Chini, M., Corato, G., Schlaffer, S., Matgen, P., 2016. Probabilistic flood mapping using synthetic aperture radar data. *IEEE Trans. Geosci. Remote Sens.* 54 (12), 6958–6969.

Gonzalez, R.C., Woods, R.E., 2007. *Digital image processing*, 2nd Edition. Prentice Hall 2011 80758.

Google Earth Engine, Google <https://earthengine.google.com/>.

Grandoni, D., 2013. Advantages and limitations of using satellite images for flood mapping. Retrieved from http://www.copernicus.eu/sites/default/files/documents/User_update/Emergency_Events/Athens/03_Session_01_AdvantageAndLimitationsOfUsingSatelliteImagery.pdf.

Grandoni, D., Battagliere, M.L., Daraio, M.G., Sacco, P., Coletta, A., Di Federico, A., Mastracci, F., 2014. Space-based technology for emergency management: the COSMO-SkyMed constellation contribution. *Procedia Technol.* 16, 858–866. <http://dx.doi.org/10.1016/j.protc.2014.10.036>.

Hajnsek, I., Jagdhuber, T., Schön, H., Papathanassiou, K.P., 2009. Potential of estimating soil moisture under vegetation cover by means of PolSAR. *IEEE Trans. Geosci. Remote Sens.* 47, 442–454. <http://dx.doi.org/10.1109/TGRS.2008.2009642>.

Henry, J.B., Chastanet, P., Fellah, K., Desnos, Y.L., 2006. Envisat multi-polarized ASAR data for flood mapping. *Int. J. Remote Sens.* 27 (9–10), 1921–1929. <http://dx.doi.org/10.1080/01431160500486724>.

Hong, S.H., Wdowinski, S., 2014. Double-bounce component in cross-polarimetric SAR from a new scattering target decomposition. *IEEE Trans. Geosci. Remote Sens.* 52 (6), 3039–3051. <http://dx.doi.org/10.1109/TGRS.2013.2268853>.

Horritt, M.S., 1999. A statistical active contour model for SAR image segmentation. *Image Vis. Comput.* 17 (3–4), 213–224. [http://dx.doi.org/10.1016/S0262-8856\(98\)00101-2](http://dx.doi.org/10.1016/S0262-8856(98)00101-2).

Horritt, M.S., Mason, D.C., Luckman, a. J., 2001. Flood boundary delineation from synthetic aperture radar imagery using a statistical active contour model. *Int. J. Remote Sens.* 22 (October 2004), 2489–2507. <http://dx.doi.org/10.1080/0143116015297691>.

Hostache, R., Matgen, P., Wagner, W., 2012. Change detection approaches for flood extent mapping: how to select the most adequate reference image from online archives? *Int. J. Appl. Earth Obs. Geoinf.* 19 (1), 205–213. <http://dx.doi.org/10.1016/j.jag.2012.05.003>.

Hua-Dong, G., Li, Z., Lan-Wei, Z., 2015. Earth observation big data for climate change research. *Adv. Clim. Chang. Res.* 6 (2), 108–117. <http://dx.doi.org/10.1016/j.accre.2015.09.007>.

International Charter International Charter on Space and Major Disasters. <https://www.disasterscharter.org>.

Jackson, T.J., Schmugge, J., Engman, E.T., 1996. Remote sensing applications to hydrology: soil moisture. *Hydrolog. Sci. J.* 41 (4), 517–530. <http://dx.doi.org/10.1080/0262669609491523>.

Jameson, A.R., Li, F.K., Durden, S.L., Haddad, Z.S., Holt, B., Fogarty, T., ... Moore, R.K., 1997. SIR-C/X-SAR observations of rain storms. *Remote Sens. Environ.* 59 (2), 267–279. [http://dx.doi.org/10.1016/S0034-4257\(96\)00159-9](http://dx.doi.org/10.1016/S0034-4257(96)00159-9).

Jones, K., Lanthier, Y., van der Voet, P., van Valkengoed, E., Taylor, D., Fernandez-Prieto, D., 2009. Monitoring and assessment of wetlands using Earth observation: the GlobWetland project. *J. Environ. Manag.* 90, 2154–2169. <http://dx.doi.org/10.1016/j.jenvman.2007.07.037>.

Karamouz, M., Zahmatkesh, Z., Saad, T., 2013. Cloud computing in urban flood disaster management. In: World Environmental and Water Resources Congress 2013: Showcasing the Future - Proceedings of the 2013 Congress, pp. 2747–2757. Retrieved from. <http://www.scopus.com/inward/record.url?eid=2-s2.0-84887457259&partnerID=tZ0tx3y1>.

Li, N., Wang, R., Liu, Y., Du, K., Chen, J., Deng, Y., 2014. Robust river boundaries extraction of dammed lakes in mountain areas after Wenchuan earthquake from high resolution SAR images combining local connectivity and ACM. *ISPRS J. Photogramm. Remote Sens.* 94, 91–101. <http://dx.doi.org/10.1016/j.isprsjprs.2014.04.020>.

Li, Z., Yang, C., Jin, B., Yu, M., Liu, K., Sun, M., Zhan, M., 2015. Enabling big geoscience data analytics with a cloud-based, mapreduce-enabled and service-oriented workflow framework. *PLoS ONE* 10 (3), 1–23. <http://dx.doi.org/10.1371/journal.pone.0116781>.

Liu, Y., Nishiyama, S., Yano, T., 2004. Analysis of four change detection algorithms in bi-temporal space with a case study. *Int. J. Remote Sens.* 25 (11), 2121–2139. <http://dx.doi.org/10.1080/0143116031000160647>.

Long, S., Fatoyinbo, T.E., Pollici, F., 2014. Flood extent mapping for Namibia using change detection and thresholding with SAR. *Environ. Res. Lett.* 9 (3), 35002. <http://dx.doi.org/10.1088/1748-9326/9/3/035002>.

Lu, D., Maisel, P., Brondizio, E., Moran, E., 2004. Change detection techniques. *Int. J. Remote Sens.* 25 (12), 2365–2401. <http://dx.doi.org/10.1080/0143116031000139863>.

Lunetta, R.S., Johnson, D.M., Lyon, J.G., Crotwell, J., 2004. Impacts of imagery temporal frequency on land-cover change detection monitoring. *Remote Sens. Environ.* 89 (4), 444–454. <http://dx.doi.org/10.1016/j.rse.2003.10.022>.

Ma, Y., Wu, H., Wang, L., Huang, B., Ranjan, R., Zomaya, A., Jie, W., 2015. Remote sensing big data computing: challenges and opportunities. *Futur. Gener. Comput. Syst.* 51, 47–60. <http://dx.doi.org/10.1016/j.future.2014.10.029>.

Mahmood, A., 2012. Monitoring disasters with a constellation of satellites-type examples from the international charter “space and major disasters”. *Geocarto Int.* 27 (2), 91–101. <http://dx.doi.org/10.1080/10106049.2011.622051>.

Malawi, P.D.N.A., 2015. *Malawi 2015 Floods Post Disaster Needs Assessment Report*. Government of Malawi.

Manjusree, P., Prasanna Kumar, L., Bhatt, C.M., Rao, G.S., Bhanumurthy, V., 2012. Optimization of threshold ranges for rapid flood inundation mapping by evaluating backscatter profiles of high incidence angle SAR images. *Int. J. Disaster Risk Sci.* 3 (2), 113–122. <http://dx.doi.org/10.1007/s13753-012-0011-5>.

Martinez, J.M., Le Toan, T., 2007. Mapping of flood dynamics and spatial distribution of vegetation in the Amazon floodplain using multitemporal SAR data. *Remote Sens. Environ.* 108 (3), 209–223. <http://dx.doi.org/10.1016/j.rse.2006.11.012>.

Martinis, S., Twele, A., Voigt, S., 2009. Towards operational near real-time flood detection using a split-based automatic thresholding procedure on high resolution TerraSAR-X data. *Nat. Hazards Earth Syst. Sci.* 9 (2), 303–314. <http://dx.doi.org/10.5194/nhess-9-303-2009>.

Martinis, S., Twele, A., Voigt, S., 2011. Unsupervised extraction of flood-induced backscatter changes in SAR data using markov image modeling on irregular graphs. *IEEE Trans. Geosci. Remote Sens.* 49, 251–263. <http://dx.doi.org/10.1109/TGRS.2010.2052816>.

Martinis, S., Kersten, J., Twele, A., 2015. A fully automated TerraSAR-X based flood service. *ISPRS J. Photogramm. Remote Sens.* 104, 203–212. <http://dx.doi.org/10.1016/j.isprsjprs.2014.07.014>.

Marzano, F.S., Mori, S., Weinman, J.A., Montopoli, M., 2011. Modeling polarimetric response of spaceborne synthetic aperture radar due to precipitating clouds from X- to Ka-band. *IEEE Trans. Geosci. Remote Sens.* 50 (3), 687–703. <http://dx.doi.org/10.1109/TGRS.2011.2163942>.

Mason, D.C., Horritt, M.S., Dall'Amico, J.T., Scott, T.R., Bates, P.D., 2007. Improving river flood extent delineation from synthetic aperture radar using airborne laser altimetry. *IEEE Trans. Geosci. Remote Sens.* 45 (12), 3932–3943. <http://dx.doi.org/10.1109/TGRS.2007.901032>.

Mason, D.C., Davenport, I.J., Neal, J.C., Schumann, G.J.-P., Bates, P.D., 2012a. Near real-time flood detection in urban and rural areas using high-resolution synthetic aperture radar images. *IEEE Trans. Geosci. Remote Sens.* 50 (8), 3041–3052. <http://dx.doi.org/10.1109/TGRS.2011.2178030>.

Mason, D.C., Schumann, G.J.P., Neal, J.C., Garcia-Pintado, J., Bates, P.D., 2012b. Automatic near real-time selection of flood water levels from high resolution Synthetic Aperture Radar images for assimilation into hydraulic models: a case study. *Remote Sens. Environ.* 124, 705–716. <http://dx.doi.org/10.1016/j.rse.2012.06.017>.

Matgen, P., Schumann, G., Henry, J.-B., Hoffmann, L., Pfister, L., 2007. Integration of SAR-derived river inundation areas, high-precision topographic data and a river flow model toward near real-time flood management. *Int. J. Appl. Earth Obs. Geoinf.* 9 (3), 247–263. <http://dx.doi.org/10.1016/j.jag.2006.03.003>.

Matgen, P., Hostache, R., Schumann, G., Pfister, L., Hoffmann, L., Savenije, H.H.G., 2011. Towards an automated SAR-based flood monitoring system: lessons learned from two case studies. *Phys. Chem. Earth* 36 (7–8), 241–252. <http://dx.doi.org/10.1016/j.pce.2010.12.009>.

Mertes, L.A.K., 2002. Remote sensing of riverine landscapes. *Freshw. Biol.* 47 (4), 799–816. <http://dx.doi.org/10.1046/j.1365-2427.2002.00909.x>.

Munich RE, 2014. *Loss Events Worldwide 2014 Percentage Distribution*.

Mysiak, J., Luther, J., 2013. Towards a potential European flood impact database. In: EEA – JRC – ETC/CCA Joint Technical Paper.

Nico, G., Pappalepore, M., Pasquarello, G., Refice, A., Samarelli, S., 2000. Comparison of SAR amplitude vs. coherence flood detection methods - a GIS application. *Int. J. Remote Sens.* 21 (8), 1619–1631. <http://dx.doi.org/10.1080/014311600209931>.

O'Grady, D., Leblanc, M., Gillieson, D., 2011. Use of ENVISAT ASAR Global Monitoring Mode to complement optical data in the mapping of rapid broad-scale flooding in Pakistan. *Hydrol. Earth Syst. Sci.* 15 (11), 3475–3494. <http://dx.doi.org/10.5194/hess-15-3475-2011>.

Paloscia, S., Pettinato, S., Santi, E., Notarnicola, C., Pasolli, L., Repucci, A., 2013. Soil moisture mapping using Sentinel-1 images: algorithm and preliminary validation. *Remote Sens. Environ.* 134, 234–248. <http://dx.doi.org/10.1016/j.rse.2013.02.027>.

Pierdicca, N., Pulvirenti, L., Chini, M., Guerriero, L., Candela, L., 2013. Observing floods from space: experience gained from COSMO-SkyMed observations. *Acta Astronaut.* 84, 122–133. <http://dx.doi.org/10.1016/j.actaastro.2012.10.034>.

Polverari, F., Mori, S., Pierdicca, N., Marzano, F.S., Pulvirenti, L., 2014. Precipitation signature on side-looking aperture radar imaging: sensitivity analysis to surface effects at C, X and Ku band. In: European Microwave Week 2014: “Connecting the Future”, EuMW 2014 - Conference Proceedings; EuRAD 2014: 11th European Radar Conference, pp. 197–200. <http://dx.doi.org/10.1109/EuRAD.2014.6991241>.

Potin, P., Rosich, B., Miranda, N., Grimont, P., Bargellini, P., Monjoux, E., ... Krassenburg, M., 2015. Sentinel-1 mission status. In: International Geoscience and Remote Sensing Symposium (IGARSS) (Vol. 2015–Novem), pp. 2820–2823. <http://dx.doi.org/10.1109/IGARSS.2015.7326401>.

Pulvirenti, L., Pierdicca, N., Chini, M., Guerriero, L., 2011. An algorithm for operational flood mapping from Synthetic Aperture Radar (SAR) data using fuzzy logic. *Nat. Hazards Earth Syst. Sci.* 11, 529–540. <http://dx.doi.org/10.5194/nhess-11-529-2011>.

Pulvirenti, L., Chini, M., Marzano, F.S., Pierdicca, N., Mori, S., Guerriero, L., ... Candela, L., 2012. Detection of floods and heavy rain using Cosmo-SkyMed data: the event in Northwestern Italy of November 2011. In: International Geoscience and Remote Sensing Symposium (IGARSS), (November 2011), pp. 3026–3029. <http://dx.doi.org/10.1109/IGARSS.2012.6350788>.

Pulvirenti, L., Pierdicca, N., Chini, M., Guerriero, L., 2013. Monitoring flood evolution in vegetated areas using cosmo-skymed data: the tuscany 2009 case study. *IEEE J. Sel. Top. Appl. Earth Obs. Remote Sens.* 6 (4), 1807–1816. <http://dx.doi.org/10.1109/JSTARS.2012.2219509>.

Pulvirenti, L., Marzano, F.S., Pierdicca, N., Mori, S., Chini, M., 2014. Discrimination of water surfaces, heavy rainfall, and wet snow using COSMO-SkyMed observations of severe weather events. *IEEE Trans. Geosci. Remote Sens.* 52 (2), 858–869. <http://dx.doi.org/10.1109/TGRS.2013.2244606>.

Pulvirenti, L., Chini, M., Pierdicca, N., Boni, G., 2016. Use of SAR data for detecting floodwater in urban and agricultural areas: the role of the interferometric coherence. *IEEE Trans. Geosci. Remote Sens.* 54 (3), 1532–1544. <http://dx.doi.org/10.1109/TGRS.2015.2482001>.

Quesney, A., Le Hégaret-Mascle, S., Taconet, O., Vidal-Madjar, D., Wigneron, J.P., Loumagne, C., Normand, M., 2000. Estimation of watershed soil moisture index from ERS/SAR data. *Remote Sens. Environ.* 72 (3), 290–303. [http://dx.doi.org/10.1016/S0034-4257\(99\)00102-9](http://dx.doi.org/10.1016/S0034-4257(99)00102-9).

Schabert, G.G., McCauley, J.F., Breed, C.S., 1997. The use of multifrequency and polarimetric SIR-C/X-SAR data in geologic studies of Bir Safsaf, Egypt. *Remote Sens. Environ.* 59 (2), 337–363. [http://dx.doi.org/10.1016/S0034-4257\(96\)00143-5](http://dx.doi.org/10.1016/S0034-4257(96)00143-5).

Schlaffer, S., Chini, M., Giustarini, L., Matgen, P., 2017. Probabilistic mapping of flood-induced backscatter changes in SAR time series. *Int. J. Appl. Earth Obs. Geoinf.* 56, 77–87. <http://dx.doi.org/10.1016/j.jag.2016.12.003>.

Schumann, G., Bates, P.D., Horritt, M.S., Matgen, P., Pappenberger, F., 2009. Progress in integration of remote sensing-derived flood extent and stage data and hydraulic models. *Rev. Geophys.* 47 (3). <http://dx.doi.org/10.1029/2008RG000274>.

Schumann, G., Di Baldassarre, G., Alsdorf, D., Bates, P.D., 2010. Near real-time flood wave approximation on large rivers from space: application to the River Po, Italy. *Water Resour. Res.* 46 (5), 1–8. <http://dx.doi.org/10.1029/2008WR007672>.

Scorzini, A.R., Frank, E., 2015. Flood damage curves: new insights from the 2010 flood in Veneto, Italy. *J. Flood Risk Manage.* 1–12. <http://dx.doi.org/10.1111/jfr3.12163>.

Shoshany, M., et al., 2000. The relationship between ERS-2 SAR backscatter and soil moisture: generalization from a humid to semi-arid transect. *Int. J. Remote Sens.* 21 (11), 2337–2343.

Singh, A., 1989. Review article digital change detection techniques using remotely-sensed data. *Int. J. Remote Sens.* 10 (6), 989–1003. <http://dx.doi.org/10.1080/01431168908903939>.

Smith, L.C., 1997. Satellite remote sensing of river inundation area, stage, and discharge: a review. *Hydrol. Process.* 11 (10), 1427–1439. [http://dx.doi.org/10.1002/\(sici\)1099-1085\(199708\)11:10<1427::aid-hyp473>3.0.co;2-s](http://dx.doi.org/10.1002/(sici)1099-1085(199708)11:10<1427::aid-hyp473>3.0.co;2-s).

Torres, R., Snoeij, P., Geudtner, D., Bibby, D., Davidson, M., Attema, E., ... Rostan, F., 2012. GMES Sentinel-1 mission. *Remote Sens. Environ.* 120, 9–24. <http://dx.doi.org/10.1016/j.rse.2011.05.028>.

Townsend, P.A., 2002. Estimating forest structure in wetlands using multitemporal SAR. *Remote Sens. Environ.* 79 (2–3), 288–304. [http://dx.doi.org/10.1016/S0034-4257\(01\)00280-2](http://dx.doi.org/10.1016/S0034-4257(01)00280-2).

Twele, A., Cao, W., Plank, S., Martinis, S., 2016. Sentinel-1-based flood mapping: a fully automated processing chain. *Int. J. Remote Sens.* 37 (13), 2990–3004. <http://dx.doi.org/10.1080/01431161.2016.1192304>.

Ulaby, F.T., Dobson, M.C., 1989. *Handbook of Radar Scattering Statistics for Terrain Data Base (Vol. 1)*. UNISDR, 2015. Sendai Framework for Disaster Risk Reduction - UNISDR, (March). pp. 1–25. <https://doi.org/A/CONF.224/CRP.1>.

van Zyl, J.J., Zebker, H.A., Elachi, C., 1987. Imaging radar polarization signatures: theory and observation. *Radio Sci.* 22 (4), 529–543. <http://dx.doi.org/10.1029/RS022i004p00529>.

Waisurasingha, C., Aniya, M., Hirano, A., Kamusoko, C., Sommut, W., 2007. Application of C-band Synthetic Aperture Radar Data and Digital Elevation Model to Evaluate the Conditions of Flood-affected Paddies: Chi River Basin, Thailand. *Asian Association on Remote Sensing, Proceedings ACRS*.

W., Wagner, Lemoine, G., Rott, H., 1999. A method for estimating soil moisture from ERS scatterometer and soil data. *Remote Sens. Environ.* 70 (2), 191–207.

Ward, D.P., Petty, A., Setterfield, S.A., Douglas, M.M., Ferdinand, K., Hamilton, S.K., Phinn, S., 2014. Floodplain inundation and vegetation dynamics in the Alligator Rivers region (Kakadu) of northern Australia assessed using optical and radar remote sensing. *Remote Sens. Environ.* 147, 43–55. <http://dx.doi.org/10.1016/j.rse.2014.02.009>.

Wilson, B.A., Rashid, H., 2005. Monitoring the 1997 flood in the Red River valley. *Can. Geogr.* 49 (1), 100–109.

Yang, C., Xu, Y., Nebert, D., 2013. Redefining the possibility of digital earth and geosciences with spatial cloud computing. *Int. J. Digital Earth* 6 (4), 297–312. <http://dx.doi.org/10.1080/17538947.2013.769783>.

Yang, C., Huang, Q., Li, Z., Liu, K., Hu, F., 2017. Big data and cloud computing: innovation opportunities and challenges. *Int. J. Digital Earth* 10 (1), 13–53. <http://dx.doi.org/10.1080/17538947.2016.1239771>.

Yue, P., Zhou, H., Gong, J., Hu, L., 2013. Geoprocessing in cloud computing platforms – a comparative analysis. *Int. J. Digital Earth* 6 (March 2015), 404–425. <http://dx.doi.org/10.1080/17538947.2012.748847>.